

submitted to ApJ

On the Redshift Distribution of Gamma-Ray Bursts in the Swift Era

Truong Le¹ and Charles D. Dermer²

E.O. Hulbert Center for Space Research

Naval Research Laboratory,

Washington, DC 20375, USA

ABSTRACT

A simple physical model for long-duration gamma-ray bursts (GRBs) is used to fit the redshift (z) and the jet opening-angle distributions measured with earlier GRB missions and with Swift. The effect of different sensitivities for GRB triggering is sufficient to explain the difference in the z distributions of the pre-Swift and Swift samples, with mean redshifts of $h_{\text{z1}} = 1.4$ and $h_{\text{z2}} = 2.8$, respectively. Assuming that the emission properties of GRBs do not change with time, we find that the data can only be fitted if the comoving rate-density of GRB sources exhibits positive evolution to $z \approx 3 \pm 5$. The mean intrinsic beaming factor of GRBs is found to range from 34 ± 42 , with the Swift average opening half-angle $h_{\text{ji}} = 10^\circ$, compared to the pre-Swift average of $h_{\text{ji}} = 7^\circ$. Within the uniform jet model, the GRB luminosity function is $\propto L^{-3.25}$, as inferred from our best fit to the opening angle distribution. Because of the unlikely detection of several GRBs with $z < 0.25$, our analysis indicates that low redshift GRBs represent a different population of GRBs than those detected at higher redshifts. Neglecting possible metallicity effects on GRB host galaxies, we find that ≈ 1 GRB occurs every 600,000 yrs in a local spiral galaxy like the Milky Way. The fraction of high-redshift GRBs is estimated at 8 ± 12% and 2.5 ± 6% at $z = 5$ and $z = 7$, respectively, assuming continued positive evolution of the GRB rate density to high redshifts.

Subject headings: gamma-rays: bursts | cosmology: theory

1. INTRODUCTION

Gamma-ray bursts (GRBs) are brief flashes of rays occurring at an average rate of a few per day throughout the universe. The ultimate energy source of a GRB is believed to be associated

¹truong.le@nrlnavy.mil²dermer@gamma.nrlnavy.mil

with a catastrophic event associated with black-hole formation (Meszaros & Rees 1997). This event takes place through the collapse of the core of a massive star in the case of long-duration GRBs, and due to merger or accretion-induced collapse events for the short-hard class of GRBs. For the class of long-duration GRBs, which is the only type considered in this paper, liberation of energy from the GRB source is thought to result in a very high temperature, baryon-dilute fireball that expands to reach highly relativistic speeds and form a collimated outflow. Dissipation of the directed kinetic energy of the relativistic blast wave through internal and external shocks is the standard model for producing the prompt radiation and afterglow (see Meszaros 2006, for a recent review).

Evidence of jetted GRBs is obtained from radio (Waxman, Kulkarni & Frail 1998) and optical (Stanek et al. 1999) observations of achromatic breaks in the afterglow light curves. The structure of these jets is, however, still an open question. The two leading models are (1) the uniform jet model, in which the energy per solid angle $\Omega E = \Omega$ is roughly constant within a well-defined jet opening angle θ_j , but drops sharply outside of θ_j , with θ_j differing between GRBs (see Meszaros, Rees & Wijers 1998; Meszaros & Rees 1997); and (2) the universal structured jet model (Rossi, Lazzati & Rees 2002; Zhang et al. 2004), in which all GRB jets are intrinsically identical with the directional energy release $\Omega E = \Omega$ dropping approximately as the inverse square of the opening angle from the jet axis.

Frail et al. (2001) and Panaitescu & Kumar (2001) found that the absolute γ -ray energy releases, after correcting for the jet opening angles inferred from the afterglow light curves, are clustered near $E = 5 \times 10^{50}$ ergs. Bloom et al. (2003), treating a larger sample, confirmed this clustering around $E = 1.3 \times 10^{51}$ ergs (the total energy release $E = \int dE \Omega E = \Omega E > E$ depends on the assumed efficiency for γ -ray energy conversion). In a later analysis by Friedman & Bloom (2005), still in the pre-Swift era, a broader spread by about one order of magnitude is found in the beam-corrected γ -ray energy release around a mean value of $E = 2 \times 10^{51}$ ergs (see Fig. 1). Since we use jet opening angles derived from these analyses, which are based on the uniform jet model, we also adopt this model in our treatment. The sample of Friedman & Bloom (2005) is taken to provide a good representation of the pre-Swift observations of GRBs.

GRBs can in principle be detected to very high redshift, $z \approx 10$ (Ciardi & Loeb 2000; Lamb & Reichart 2000), which holds promise that GRBs can be used to probe the early universe. Their utility for this purpose depends on the frequency and brightness of high-redshift GRBs, which in turn depends on the rate-density evolution of GRB sources and the evolution of GRB source properties with cosmic time. Given the assumption that the GRB rate density is proportional to the measured star formation rate (SFR) history of the universe (Totani 1999; Blain & Narayan 2000), the redshift distribution of GRBs can be predicted (Bromm & Loeb 2002). Correlations between spectral properties and energy releases may also permit GRBs to be used to determine cosmological parameters (e.g., Ghirlanda et al. 2004; Mortsell & Sollerman 2005).

With the launch of the Swift satellite (Gehrels et al. 2004), rapid follow-up studies of GRBs triggered by the Burst Alert Telescope (BAT) on Swift became possible. A fainter and more

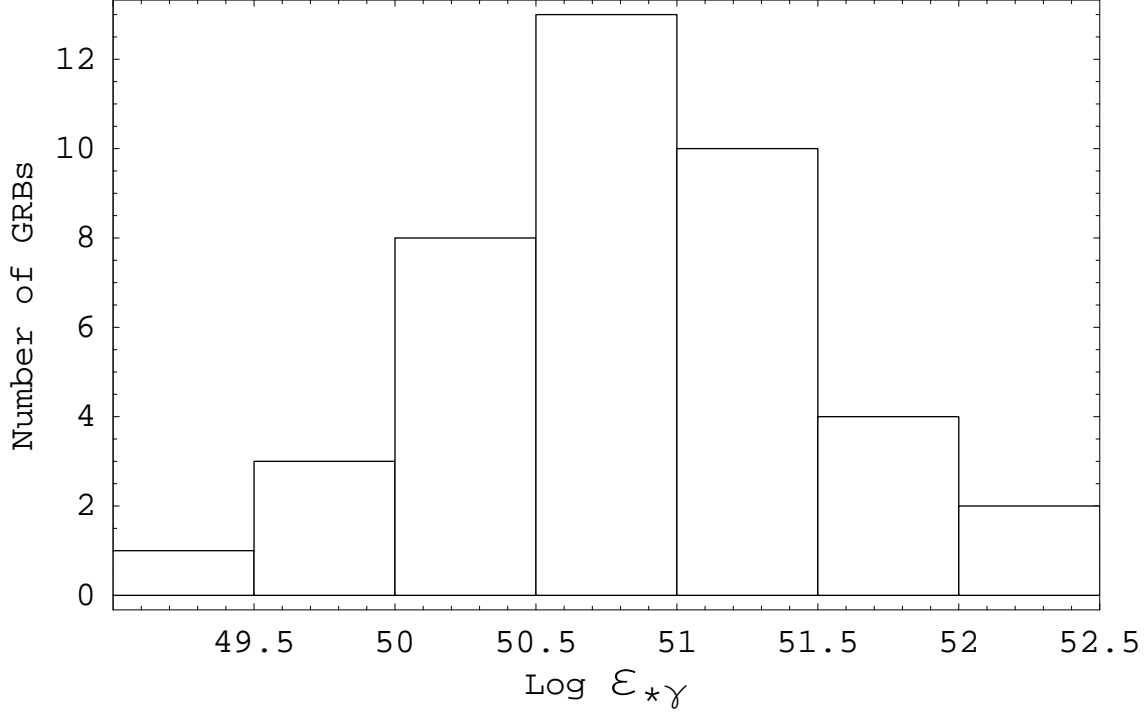


Fig. 1.1| Histogram of the corrected absolute γ -ray energy release E^* for pre-Swift GRBs (Friedman & Bloom 2005).

distant population of GRBs than found with the pre-Swift satellites CGRO-BATSE, BeppoSAX, INTEGRAL, and HETE-2 is detected (Berger et al. 2005). The mean redshift of 41 pre-Swift GRBs that also have measured beaming breaks (Friedman & Bloom 2005) is $h_{\text{z}} = 1.4$, while 31 GRBs discovered by Swift have $h_{\text{z}} = 2.8$ (Jakobsson et al. 2006) (see Fig. 2). Bagoly et al. (2006) performed five different statistical tests to compare the redshift distributions of Swift and pre-Swift GRBs assuming, as the null hypothesis, that they are identical distributions. They conclude that the redshift distributions are different, that is, all five tests reject the null hypothesis at the 97% significance level. Thus, this suggests that the pre-Swift and Swift satellites sample different (though possibly overlapping) GRB populations.

Here, we develop a physical model to understand the difference between the redshift distributions of Swift and pre-Swift GRBs, taking into account the different detector triggering properties. The GRB model is based on the uniform jet model for GRBs, though the typical properties are assigned in accordance with GRB observations. The GRB rate density and distribution of jet opening angles are the principle unknowns, with parameter values for the mean intrinsic duration and absolute γ -ray energy release of GRBs determined from observations and best fits to the data. A GRB is detected if its flux exceeds the flux threshold within the energy window of a detector (the actual detection criteria are more complicated; see Band 2003, 2006, and discussion below). For a

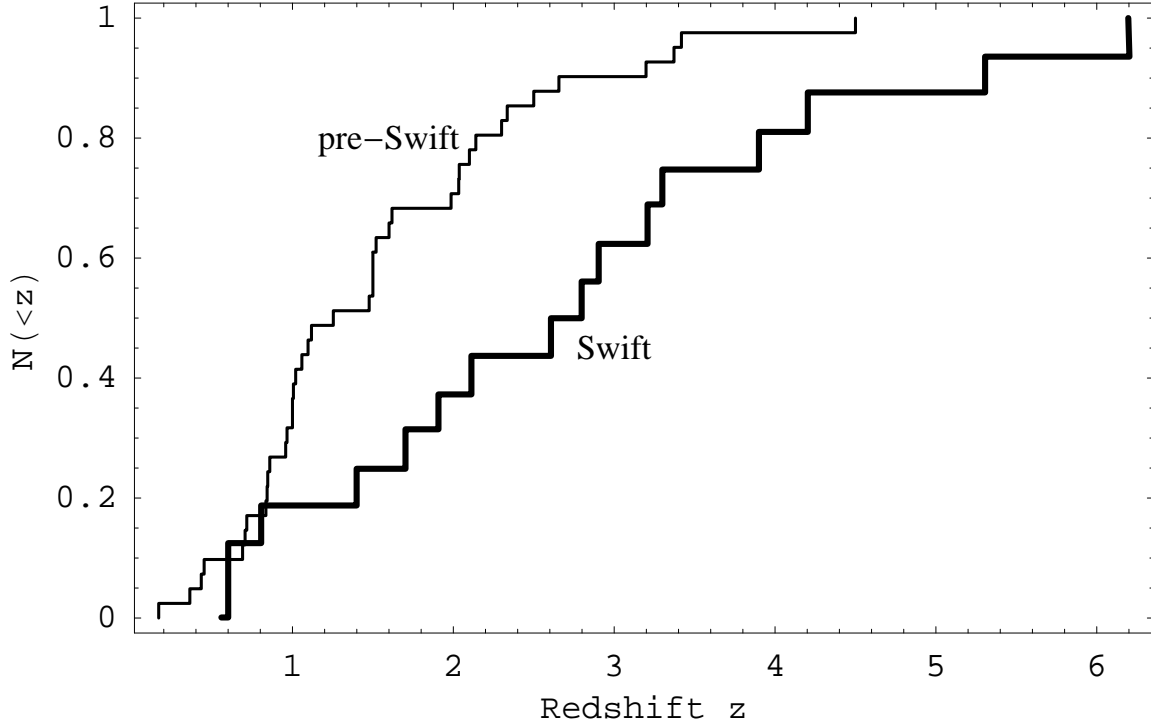


Fig. 2. The cumulative redshift distribution of GRBs for 41 GRBs in the pre-Swift sample (thick lines; Friedman & Bloom 2005), and 31 GRBs in the Swift sample (thin lines; Jakobsson et al. 2006). The median redshifts of the pre-Swift and Swift bursts are $z = 1.04$ and $z = 2.72$, respectively.

given rate density of GRBs, the redshift and opening angle distributions are calculated and fit to the data.

In § 2, we develop the formulation for bursting sources, and we fit the data in § 3. Inferences for the differences between the Swift and pre-Swift redshift distributions are also made in § 3, including implications for beaming factors and low- z GRBs. We conclude in § 4 by discussing the derived GRB source rate density, the nature of the low-redshift GRBs with weak energies, and the predicted fraction of high-redshift GRBs. Derivation of the bursting rate of sources in a flat cold dark matter cosmology is given in the Appendix.

2. Statistics of Cosmological GRBs

2.1. Model GRB

We approximate the spectral and temporal profiles of a GRB occurring at redshift z by an emission spectrum that is constant for observing angles $\theta = \arccos(\cos\theta_j) = \arccos(\cos\theta_j)$ to the

jet axis during the period t ; thus the duration of the GRB in the observer's frame is simply $t = (1+z)t$ (stars refer to the stationary frame, and terms without stars refer to observer quantities). The F spectrum is therefore written as

$$F = f_{pk} S(x) H(\theta_j; 1) H(t; 0; t); \quad (1)$$

where the spectral function $S(x) = 1$ at $x = \theta_{pk} = \theta_{pk}$. At observer time t , $\theta = h = m_e c^2$ is the dimensionless energy of a photon in units of the electron rest-mass energy, and θ_{pk} is the photon energy at which the energy flux f takes its maximum value f_{pk} . The quantity $H(\theta_j; 1)$ is the Heaviside function such that $H(\theta_j; 1) = 1$ when $\theta_j \leq 1$, that is, the angle of the observer with respect to the jet axis is within the opening angle of the jet, and $H(\theta_j; 1) = 0$ otherwise. One possible approximation to the GRB spectrum is a broken power law, so that

$$S(x) = \frac{a}{\theta_{pk}} H(\theta_{pk}) + \frac{b}{\theta_{pk}} H(\theta_{pk}); \quad (2)$$

where the Heaviside function $H(u)$ of a single index is defined such that $H(u) = 1$ when $u \geq 0$ and $H(u) = 0$ otherwise. The F spectral indices are denoted by $a > 0$ and $b < 0$. Note that $S(x)$ can easily be generalized to accommodate spectral energy distributions (SEDs) with multiple components.

The bolometric fluence of the model GRB for observers with θ_j is given by

$$F = \int_1^{\theta_j} dt \int_0^{\theta_{pk}} d\theta \frac{f(t)}{1+z} = f_{pk} t; \quad (3)$$

where f_{pk} is a bolometric correction to the peak measured flux. If the SED is described by eq. (2), then $f_{pk} = (a^1 - b^1)$, and is independent of θ_{pk} . The beaming-corrected ray energy release E for a two-sided jet is given by

$$E = 4 \pi d_L^2 (1 - \theta_j) \frac{F}{1+z}; \quad (4)$$

where the luminosity distance

$$d_L(z) = \frac{c}{H_0} (1+z) \int_0^z \frac{dz^0}{(1+z^0)^3 + p_m}; \quad (5)$$

for a CDM universe. Substituting eq. (3) for F into eq. (4) gives

$$f_{pk} = \frac{E}{4 \pi d_L^2 (1 - \theta_j) t} : \quad (6)$$

Finally, by substituting eq. (6) into eq. (1), the energy flux becomes

$$f(t) = \frac{E}{4 \pi d_L^2 (1 - \theta_j) t} H(t; 0; t) S(x) : \quad (7)$$

A at F spectrum ($a = b = 0$) has to be cut off at low and high energies in order to avoid divergent flux. In this paper we consider the simplest GRB SED with $a = b = 0$, such that $b \neq \ln(x_{\text{max}}/x_{\text{min}})$, with the at part of the spectrum assumed to intersect with the sensitive range of the GRB detector. The model spectrum is not likely to extend over more than two orders of magnitude, so that $b \leq 5$. Thus we take b , the bolometric correction factor, equal to 5 in our calculations.

2.2. Bursting Rate of GRB Sources

To calculate the redshift and the jet opening angle distributions, we need to determine the rate at which GRBs occur per steradian. For a CDM cosmology with $\Omega_m = 0.27$, $\Omega_b = 0.73$, and $H_0 = 72 \text{ km s}^{-1} \text{ Mpc}^{-1}$ (Spergel et al. 2003), the event rate per unit time per sr for bursting sources is

$$\frac{dN}{dt} = \frac{c}{H_0} \frac{d_L^2(z) n_{\infty}(E; j; p_k; t; z) dE}{(1+z)^3} \frac{d_j d_{p_k} d(t) dz}{m (1+z)^3} ; \quad (8)$$

(the derivation of this result is given in Appendix A). Here, $n_{\infty}(E; j; p_k; t; z) = n_{\infty}(z) Y(E; j; p_k; t)$ is the distribution of GRB sources differential in $E; j; p_k; t$; and z , and separability of the comoving rate density $n_{\infty}(z) = n_{\infty, \text{SFR}}(z)$ of GRBs from their properties is assumed, where $n_{\infty, \text{SFR}}(z)$ is GRB star formation rate function. This is the crucial assumption of this treatment, and so needs restated. There is assumed to be no evolution of the emission properties of GRB with cosmic time. Thus, for example, the mean jet opening angles, the mean energies, and the mean values of p_k (which could be correlated with E to satisfy the Amati et al. (2002) and Ghirlanda et al. (2004) relations) do not change through cosmic time. The phenomenological validity of the the Amati and Ghirlanda relations for GRBs at different values of z suggests the plausibility of this assumption. These relations can be introduced in more detailed treatments by considering source spectral properties where p_k is correlated with E .

Employing an integral formulation for beamed sources (Demberg 1992, 2006), the observed directional event rate for bursting sources¹ with F spectral flux greater than \hat{f} at observed photon energy is given by

$$\frac{dN(>\hat{f})}{dt} = \frac{c}{H_0} \frac{Z_1}{\hat{f}} \frac{df}{dz} \int_0^{Z_1} dE \int_0^{Z_1} dp_k \int_0^{Z_1} d(t) \int_{j_{\text{min}}}^{j_{\text{max}}} d_j \int_j^{Z_1} d_j \int_0^{Z_1} dz \frac{d_L^2(z) n_{\infty}(z) Y(E; j; p_k; t; z)}{(1+z)^3} \int_{\hat{f}}^{h_f} f(z; E; j; p_k; t) dz : \quad (9)$$

¹ In a more accurate treatment of detector response, one should calculate a photon-energy integration over the energy-dependent effective area, rather than describing a -ray telescope by a F flux sensitivity \hat{f} by the mean photon energy of the sensitive waveband of the detector. A further complication, not considered here, is that \hat{f} may depend on the duration t of the GRB.

This expression can also be written in terms of a Heaviside function involving a minimum flux threshold condition $f \geq \hat{f}$. For discrete values of E , p_k , and t ,

$$Y(E; j; p_k; t) = g(j) \cdot (E - E_0) \cdot (p_k - p_{k0}) \cdot (t - t_0); \quad (10)$$

where $g(j)$ is the jet opening angle distribution, and \hat{f} is the instrument's detector sensitivity. The sensitivity of a detector to a GRB depends on many factors, namely, the detector area, the detector efficiency, the fraction of the detector that is active, the fraction of the coded mask that is open, the average solid angle, and the internal background (Band 2003). Gehrels et al. (2004) give the BAT's instrument detector sensitivity to be about 10^8 ergs cm⁻² s⁻¹, which is far more sensitive than BATSE and Beppo-SAX, particularly in the case of those GRBs for which redshifts were obtained.

We can make a rough estimate of the detector threshold for both Swift and pre-Swift instruments, noting that the mean area size $h_i = u_m^{-1} = (u - 1)$ for a power law size distribution with index $u > 1$; $u = 3/2$ for a Euclidean distribution). For Swift GRBs, we took the ratio of the measured GRB fluences to their t_{90} durations² to find that the mean flux of a detected Swift GRB is $5 \cdot 10^8$ ergs cm⁻² s⁻¹. For an index $u = 1.1 \div 1.2$, as appropriate to the Swift range, we find that the Swift is sensitive to GRBs as weak as 10^8 ergs cm⁻² s⁻¹. We take this energy flux as the effective Swift flux threshold, recognizing that the actual detection of GRBs with Swift is more complicated, involving both a rate and image trigger (Band 2006).

The assignment of an effective flux threshold for the pre-Swift detectors is complicated by the fact that they involve a variety of detectors (BATSE, Beppo-SAX, HETE-II, and INTEGRAL) each with its own specific triggering criteria. The mean flux of the pre-Swift sample can be obtained from the values of fluence and t_{90} compiled by Friedman & Bloom (2005). We find that the mean flux of the pre-Swift GRBs is $7 \cdot 10^7$ ergs cm⁻² s⁻¹, meaning that the flux threshold sensitivity is a factor 5 less than this value, because $u = 1.2$ at fluxes $\approx 10^7$ ergs cm⁻² s⁻¹ (Paciesas et al. 1999). For simplicity, we use the value of 10^7 ergs cm⁻² s⁻¹ for the mean sensitivities of the GRB detectors prior to Swift. Hence, in this work we assume the detector threshold for Swift and pre-Swift GRBs to be 10^8 and 10^7 ergs cm⁻² s⁻¹, respectively.

Integrating over j in eq. (9) gives the factor $(1 - j)$ describing the rate reduction due to the finite jet opening angle. Hence, eq. (9) becomes

$$\frac{dN(\hat{f})}{d\hat{f}} = \frac{c}{H_0} \frac{Z_1}{\hat{f}} \int_{j_{in}}^0 df \int_{j_{in}}^0 dz \frac{d^2 L(z) n_{co}(z)}{(1+z)^3} \frac{(\hat{f}^0 - \hat{f})}{\hat{f}^m (1+z)^3}; \quad (11)$$

where \hat{f} is given by eq. (7).

In order to close the system of equations and solve for the redshift distribution, we must also specify the functional form of $g(j)$ as well as the comoving GRBs rate density $n_{co}(z)$. GRBs with

²swift.gsfc.nasa.gov

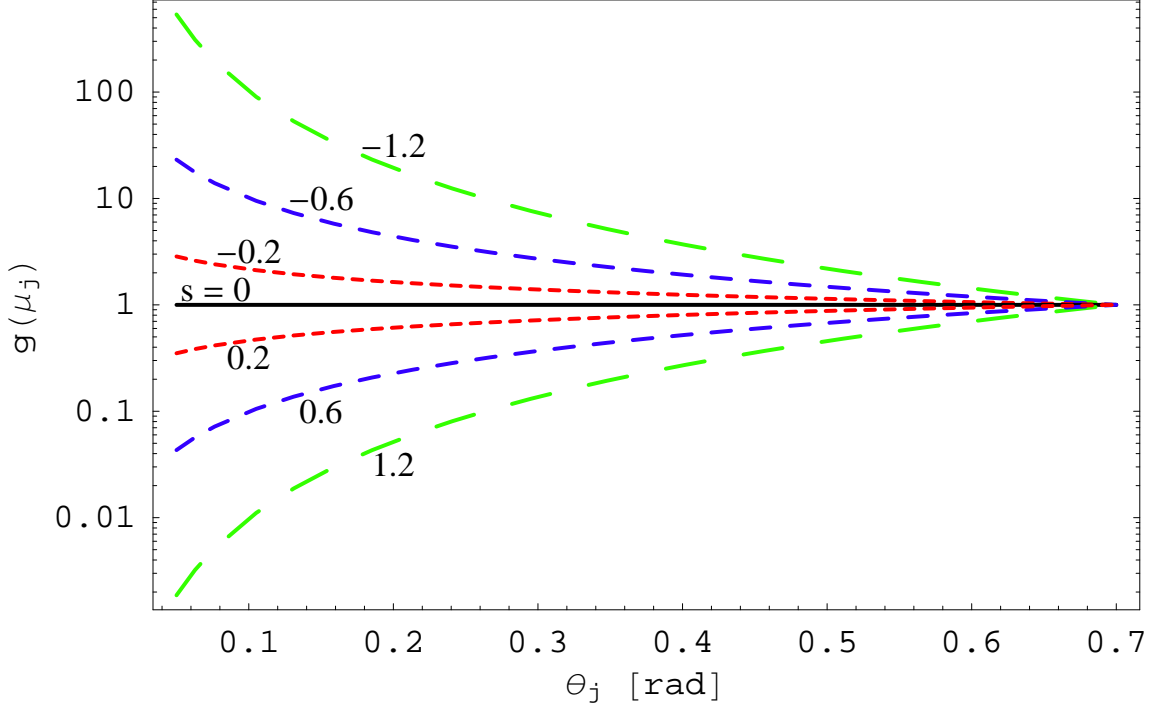


Fig. 3.1 The number of sources per unit θ_j angle for $s = -1.2, -0.6, -0.2, 0, 0.2, 0.6, 1.2$ in eq. (12) between $\theta_j = 0.05$ and 0.7 radians.

small opening angles, that is, with $\theta_j \ll 1$, will radiate their available energy into a small cone, so that such GRBs are potentially detectable from larger distances (though not always, as a different portion of the spectrum is observed), with their rate reduced by the factor $(1 - \theta_j)$. By contrast, GRB jets with large opening angles are more frequent but only detectable from comparatively small distances. The intrinsic opening angle distribution can be much different than the measured opening-angle distribution because of these effects (Guetta, Piran, & Waxman 2005).

Since the form for the jet opening angle $g(\theta_j)$ is unknown, we consider the function

$$g(\theta_j) = g_0 (1 - \theta_j)^s H(\theta_j; \theta_{\min}; \theta_{\max}); \quad (12)$$

where s is the jet opening angle power-law index; for a two-sided jet, $\theta_{\min} = 0$. Because the distributions are normalized to unity,

$$g_0 = \frac{1 + s}{(1 - \theta_{\min})^{1+s} - (1 - \theta_{\max})^{1+s}} : \quad (13)$$

Equation (12) hardly exhausts the possible expressions for $g(\theta_j)$, but contains interesting asymptotic behaviors. In Figure 3, we illustrate the nature of this function by fixing the range of the jet opening angle for different values of s . Here we take θ_j lying between 0.05 and 0.7 radians (2.8 { 40). This figure shows that the fraction of bursts with small jet opening angles $\theta_j \ll 1$

increases with decreasing values of $s < 0$. However, most bursts have large jet opening angle when $s > 0$. Since beaming effects are only important for negative s , and because beaming effects are certainly important for GRBs, we only consider negative value of s in our analysis. Furthermore, from equation (13) it is clear that if $s < -1$, it is necessary to have a minimum opening angle $j = \arccos(-s) > 0$ in order to avoid a divergent fraction of GRBs with small jet opening angles. Note also that $g(-j)$, eq. (12), approaches a δ -function when $j \rightarrow 0$.

The GRB formation history is expected to follow the cosmic SFR (SFR) derived from the blue and UV luminosity density of distant galaxies, though with differences related to the metallicity dependence and fraction of the subset of high-mass stars that are GRB progenitors. We assume that $\text{SFR}(z) / \text{SFR}_0(z)$, and consider specific functional forms for $\text{SFR}(z)$. Due to the large range of uncertainties in the SFR at $z > 1$, we first consider three different functional forms for the SFR. For the lower SFR (LSFR) and upper SFR (USFR) that should bound the actual SFR, we consider the analytic function

$$\text{SFR}(z) = \frac{1 + a_1}{(1 + z)^{a_2} + a_1(1 + z)^{a_3}}; \quad (14)$$

(Wick, Demer & Artoyan 2004), with $a_1 = 0.005(0.0001)$, $a_2 = 3.3(4.0)$, and $a_3 = 3.0(3.0)$ for the LSFR (USFR). The LSFR (SFR 2) and USFR (SFR 4) describe extreme ranges of optical/UV measurements without and with dust extinction (Blain et al. 1999) corrections, respectively. We also consider the SFR history (SFR 3) of Hopkins & Beacom (2006), which is intermediate between the LSFR and USFR, using their analytic fitting profile given by

$$\text{SFR}(z) = \frac{1 + (a_2 z - a_1)}{1 + (z - a_3)^{a_4}}; \quad (15)$$

where $a_1 = 0.015$, $a_2 = 0.10$, $a_3 = 3.4$, and $a_4 = 5.5$ are their best-fit parameters³. Figure 4 shows these SFR functions, with the function normalized to unity at the present epoch $z = 0$. The constant comoving density, SFR 1, is also plotted. Note that SFR 2, SFR 3, and SFR 4 are similar when $z < 1$, but differ greatly at higher redshifts. We also consider two alternative functions shown in Fig. 4, SFR 5 and SFR 6, that display a monotonic increase in the SFR at high redshifts representing positive evolution of the SFR history of the universe to $z > 5$. Later in the analysis we will show that for self-consistency we have to utilize SFR 5 and SFR 6 instead of SFR 2, SFR 3, and SFR 4, to obtain the best-fit to the Swift redshift, and the pre-Swift redshift and jet opening angle samples.

³Adjustments to these values in later versions of the paper by Hopkins & Beacom (2006) produce negligible differences in our results.

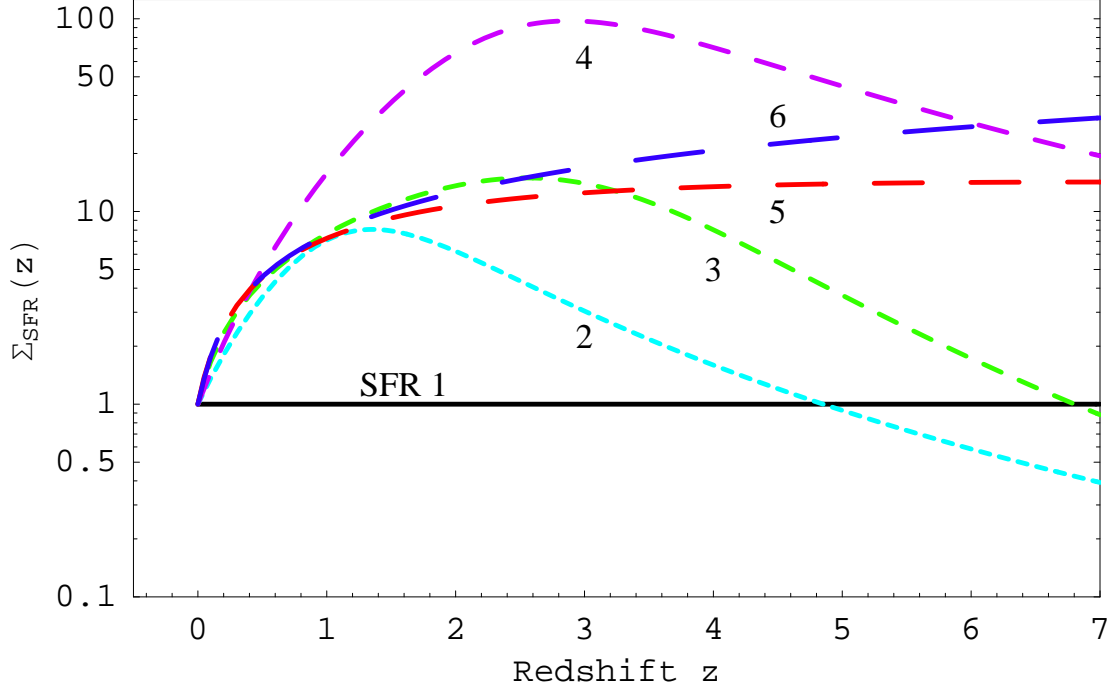


Fig. 4.| Star formation rate (SFR) function for GRBs, assumed to be proportional to comoving SFR histories as shown. The solid line (SFR 1) is a constant comoving density; SFR 2 and SFR 4 are the lower and upper SFRs given by eq. (13); SFR 3 is the Hopkins & Beacom (2006) SFR history given by eq. (14), with $a_1 = 0.015$, $a_2 = 0.1$, $a_3 = 3.4$, $a_4 = 5.5$; and SFR 5 ($a_1 = 0.015$, $a_2 = 0.12$, $a_3 = 3.0$, $a_4 = 1.3$) and SFR 6 ($a_1 = 0.011$, $a_2 = 0.12$, $a_3 = 3.0$, $a_4 = 0.5$) are the SFRs that give a good fit to the Swift and pre-Swift redshift distribution.

2.3. Redshift, Size, and Jet Opening Angle Distributions

The directional GRB rate per unit redshift with energy $ux > \hat{f}$ is thus given by

$$\frac{dN(\hat{f})}{d\hat{f} dz} = \frac{c g_0}{H_0 (2 + s)} \frac{d_L^2(z) n_{\infty}(z)}{(1 + z)^3} \frac{f_{\text{max}}^{1 + m} (1 - \frac{f}{f_{\text{max}}})^{2 + s}}{(1 - \frac{f}{f_{\text{max}}})^{2 + s} g} ; \quad (16)$$

after substituting eq. (12) into eq. (11) and solving; here

$$\hat{f}_j = 1 - \frac{E}{4 d_L^2(z) t \hat{f}_b} ; \quad (17)$$

When $f = \hat{f}$, where \hat{f} is the flux threshold sensitivity of a GRB telescope that observes in a waveband centered at λ , eq. (16) gives the redshift distribution. The size distribution of GRBs

in terms of their flux f is then simply

$$\frac{dN(\hat{f})}{d\hat{f}} = \frac{c g_0}{H_0 (2 + s)} \int_0^{z_{\text{max}}} dz \frac{d_L^2(z) n_{\infty}(z)}{(1 + z)^3} \frac{d^2_{\text{L}}(z) n_{\infty}(z)}{m (1 + z)^3} f [1 - m \text{ax}(\hat{j}; j_{\text{in}})]^{2+s} (1 - j_{\text{in}})^{2+s} g : \quad (18)$$

The maximum redshift z_{max} can be obtained by solving the luminosity distance $d_L(z)$ using equation (17) to obtain

$$d_L^2(z_{\text{max}}) = \frac{E}{4 (1 - j_{\text{in}}) t \hat{f}_b} : \quad (19)$$

Finally, the jet opening angle distribution (see eq. [11]) is given by

$$\frac{dN(\hat{f})}{d\hat{f} d_j} = \frac{c}{H_0} g(j) (1 - j) \int_0^{z_{\text{max}}(j)} dz \frac{d_L^2(z) n_{\infty}(z)}{(1 + z)^3} \frac{d^2_{\text{L}}(z) n_{\infty}(z)}{m (1 + z)^3} ; \quad (20)$$

where $g(j)$ is given in equations (12) and (13), and the upper limit of the redshift integration is determined by equation (19).

3. PARAMETER STUDY AND RESULTS

In our GRB model, there are seven adjustable parameters: the spectral power-law indices a and b , the power-law index s of the jet opening-angle distribution, the range of the jet opening angles j_{in} and j_{max} , the absolute emitted -ray energy E , and the detector threshold \hat{f} . As already mentioned, we consider, for simplicity, $a = b = 0$, leaving only the bolometric correction factor b , which is set equal to 5. The remaining parameters j_{in} , j_{max} , s , and E are constrained by observations, and the detector properties are used to estimate \hat{f} .

Besides these parameters, we must also assume a GRB comoving rate density $n_{\infty}(z) = n_{\infty} \text{SFR}(z)$, which is also constrained by fitting our model to the observed data. Adopting the uniform jet model, we assume that the energy per solid angle is roughly constant within the well-defined jet opening angle (e.g., Frail et al. 2001; Bloom et al. 2003). With these assumptions, we investigate the behavior of the redshift and opening angle distributions. Before we proceed to compare our model of redshift and jet opening angle distributions with the samples obtained by the Swift and pre-Swift instruments, we need to explore some of the above parameter space.

For illustrative purposes, we utilize SFR 3 (Hopkins & Beacom 2006) for the GRB comoving rate density. Furthermore, we also assume that $s = 0$, $j_{\text{in}} = j_{\text{max}} = j = 0.1$ radian (this assumption implies $g(j)$ is a -function, see eqs. [11], and [12]), $t = 10$ s, $E = 2 \times 10^{51}$ ergs, and $\hat{f} = 10^{-8}$ and 10^{-7} ergs $\text{cm}^{-2} \text{s}^{-1}$ for the flux sensitivity of detectors for Swift and before

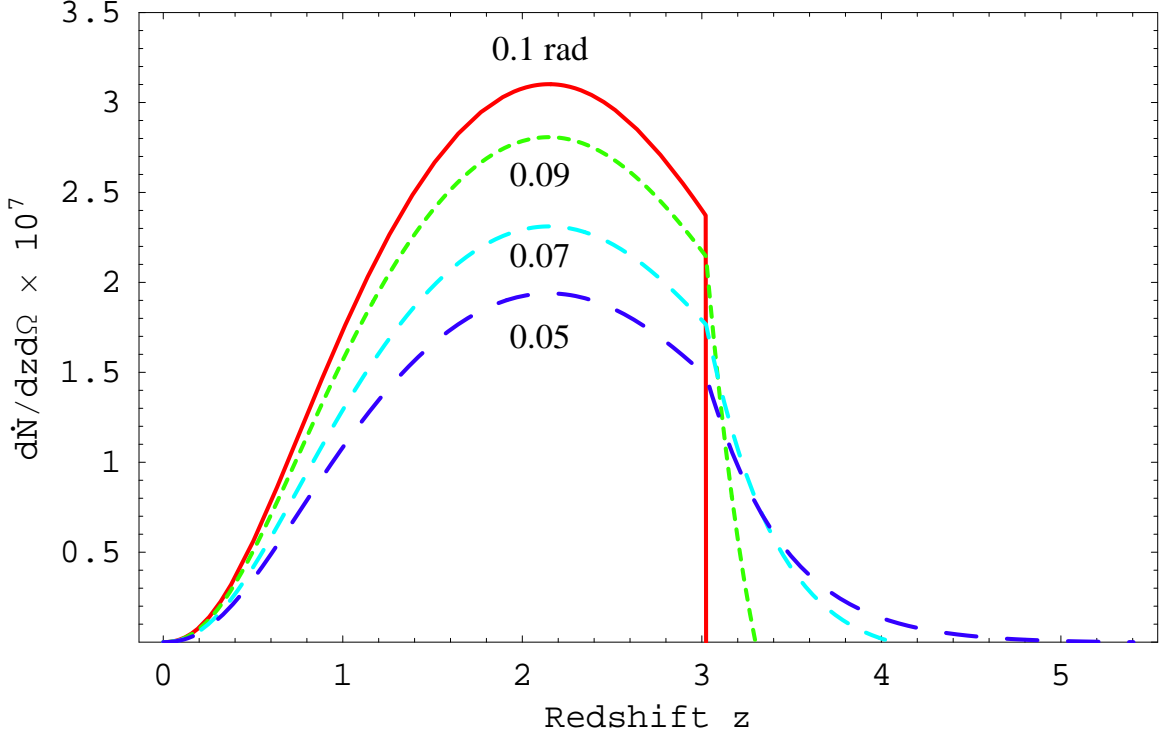


Fig. 5.1 Directional event rate per unit redshift [one event per $(10^{28} \text{ cm})^3$ per day per sr per z] for an assumed δ -function distribution of the jet opening angles, so that $g(j) = \delta(j - \hat{j})$, with $\hat{j} = 0.1$ radian (solid curve), using $\hat{f} = 10^7 \text{ ergs cm}^{-2} \text{ s}^{-1}$. Also shown are the directional event rates with $j_{\text{max}} = 0.1$ radian, and $j_{\text{min}} = 0.05, 0.07$, and 0.09 radians, with $s = 0$.

Swift, respectively. We choose $t = 10$ s, and $E = 2 \times 10^{51}$ ergs because these are the mean values of the GRB duration measured with BATSE assuming that BATSE GRBs are typically at $z = 1$, and the mean beam ing corrected γ -ray energy release (see Fig. 1), respectively. We shall use $t = 10$ s throughout this work. The calculation is normalized to a local ($z = 1$) event rate of one GRB per day per $(10^{28} \text{ cm})^3$, so that the normalization of the local rate density is $n_\infty = 1.157 \times 10^{89} \text{ cm}^{-3} \text{ s}^{-1}$.

With the jet opening angle $j = 0.05$ and $j = 0.1$ radians, and the detector threshold $\hat{f} = 10^7 \text{ ergs cm}^{-2} \text{ s}^{-1}$, the maximum redshifts from which model GRBs could be detected are $z_{\text{max}} = 5.4$ and 3.02 , respectively (see eq. [19]). The directional event rate per unit redshift is shown in Figure 5. Setting $j_{\text{max}} = 0.1$ radian, and $j_{\text{min}} = 0.05, 0.07, 0.09$ radians (the three dashed curves in Figure 5), we plot the directional event rate per unit redshift for different values of j_{min} (see eq. [18]). As $j_{\text{min}} \rightarrow j_{\text{max}}$, the directional event rate per unit redshift of the respective j_{min} -curves approaches the directional event rate per redshift of the δ -function $g(j)$ with $j = 0.1$ radian.

In Figure 6 we examine three different values of the jet opening angle, $j_{\text{min}} = j_{\text{max}} = j = 0.05, 0.1$, and 0.2 radians, with two values of flux sensitivity, namely 10^{-8} and 10^{-7} $\text{ergs cm}^{-2} \text{ s}^{-1}$. As

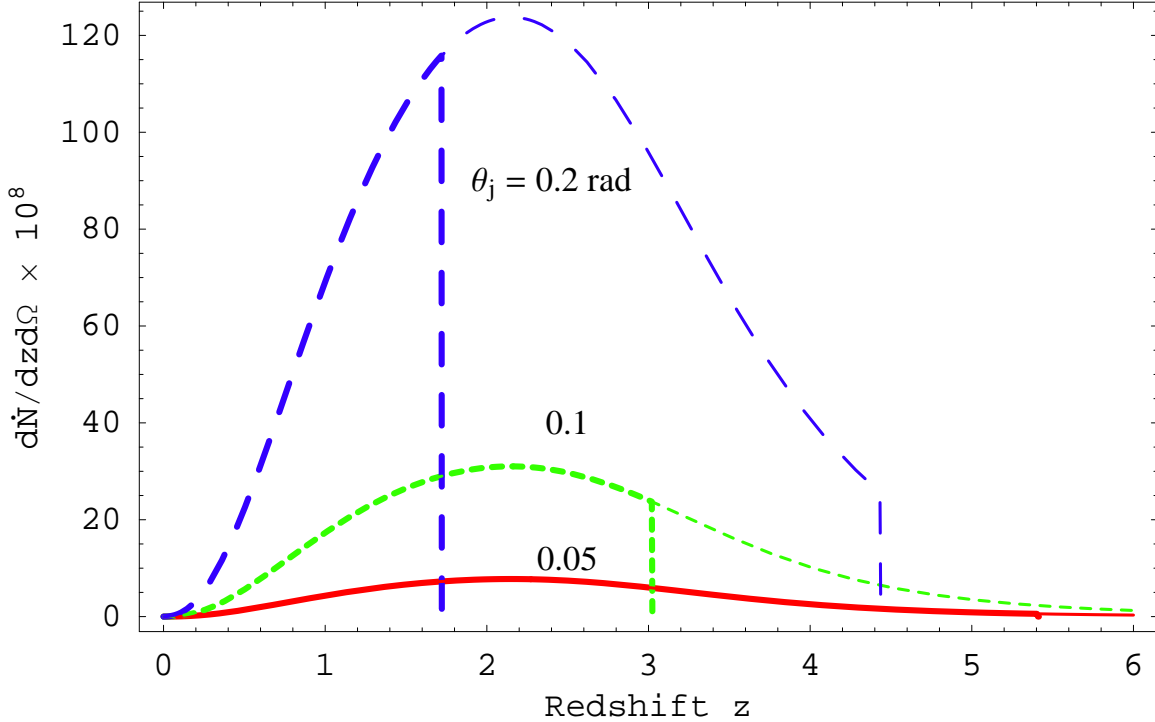


Fig. 6. Directional event rate per unit redshift, in units of GRBs per s per sr per unit redshift z , normalized to one event per $(10^{28} \text{ cm})^3$ per day, with $\theta_j = 0.05, 0.1$, and 0.2 radian, using SFR 3. The thin and thick curves represent the instrument's energy flux sensitivity of $10^{-8} \text{ ergs cm}^{-2} \text{ s}^{-1}$ (Swift) and $10^{-7} \text{ ergs cm}^{-2} \text{ s}^{-1}$ (pre-Swift), respectively.

can be seen, the smaller the jet opening angle the larger the maximum redshift from which the GRB is detectable. The maximum observable redshift z associated with a particular opening angle is indicated by the vertical line in each curve. Moreover, Figure 6 also shows that whatever the lower sensitivity telescope detects will also be detected by a telescope with better sensitivity, because a at F spectrum is considered. Thus Swift, being more sensitive than earlier telescopes, would in this model detect a sample of GRBs encompassing those detected with instruments before Swift. Spectral behavior can be considered in more detailed treatments and will change the relations for maximum distances, though generally with better sensitivity the telescope can view to larger distances, especially when the more sensitive telescope can observe lower energy photons.

By varying the opening angle power-law index parameter s over values $s = 0.0, 0.5, 0.9, 1.5, 2.5$, and 10.0 , with $j_{\text{min}} = 0.05$, $j_{\text{max}} = 0.7$ radians and $f = 10^{-8} \text{ ergs cm}^{-2} \text{ s}^{-1}$, while keeping all other assumed parameters as before, Figure 7 shows that the burst rate per unit redshift is progressively distributed to higher z , as expected, since the more negative s is, the larger is the fractional number of bursts that occurs at small jet-opening angles θ_j (see also Figure 3). More importantly, as $s \rightarrow 0$, the directional event rate per unit redshift reaches an asymptotic limit (see

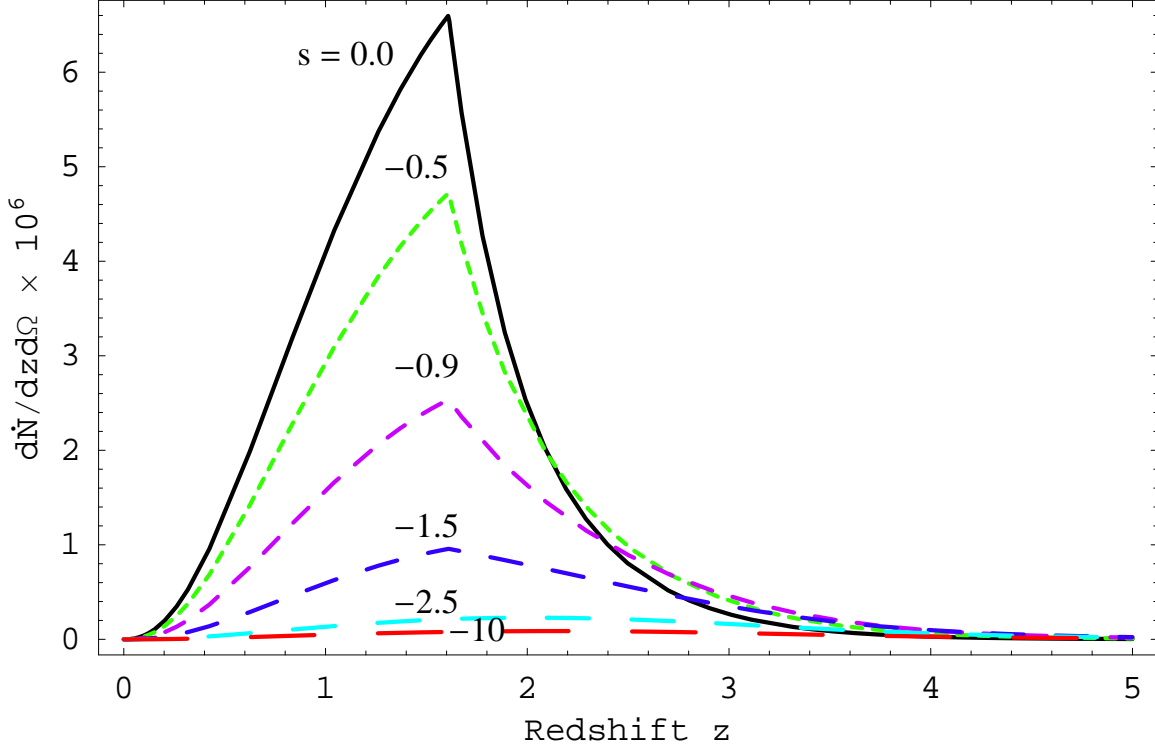


Fig. 7. Directional event rate per unit redshift with $j_{\text{in}} = 0.05$ rad and $j_{\text{max}} = 0.7$ rad, $s = 0.0, -0.5, -0.9, -1.5, -2.5$, and -10.0 , with SFR 3 and $\dot{E} = 10^8$ ergs cm $^{-2}$ s $^{-1}$.

plots for $s = -2.5$ and -10.0 in Figure 7).

The final parameter that we need to explore is the corrected γ -ray energy E . By setting $E = 5 \cdot 10^{50}, 2 \cdot 10^{51}, 4 \cdot 10^{51}$, and 10^{52} ergs with $j_{\text{in}} = 0.05$ and $j_{\text{max}} = 0.7$ radians, $s = 0$, and $\dot{E} = 10^8$ ergs cm $^{-2}$ s $^{-1}$, Figure 8 shows that as the emitted γ -ray energy increases, the bursting rate is shifted to higher z , as expected. We now proceed to investigate the parameters that best fit the Swift and pre-Swift redshift samples.

From Friedman & Bloom (2005), the pre-Swift jet opening angle distribution extends from $j = 0.05$ to $j = 0.6$ radians. However, other workers have reported that the observed jet-opening angles are as large as $j = 0.7$ radians (e.g., Guetta, Piran, & Waxman 2005). Hence, in this work we explore different ranges of j , ranging from $j_{\text{in}} = 0.05$ radians to $j_{\text{max}} = -2, 0.7$, and 0.4 radians. We also use $t = 10$ s as the average GRB duration in the stationary frame. We first consider SFR 3 (Hopkins & Beacom 2006) to fit the redshift distribution from the Swift and pre-Swift samples, and the opening angle distribution from the pre-Swift sample. A large number of jet opening angles associated with the Swift redshift sample is lacking, so our calculated jet opening angle distribution will be used as a prediction for Swift. As indicated in Figure 1, the corrected γ -ray energy release is broadly distributed around the mean value of $E = 2 \cdot 10^{51}$ ergs; hence we can explore different values of γ -ray energy that best fit the observed redshift and opening

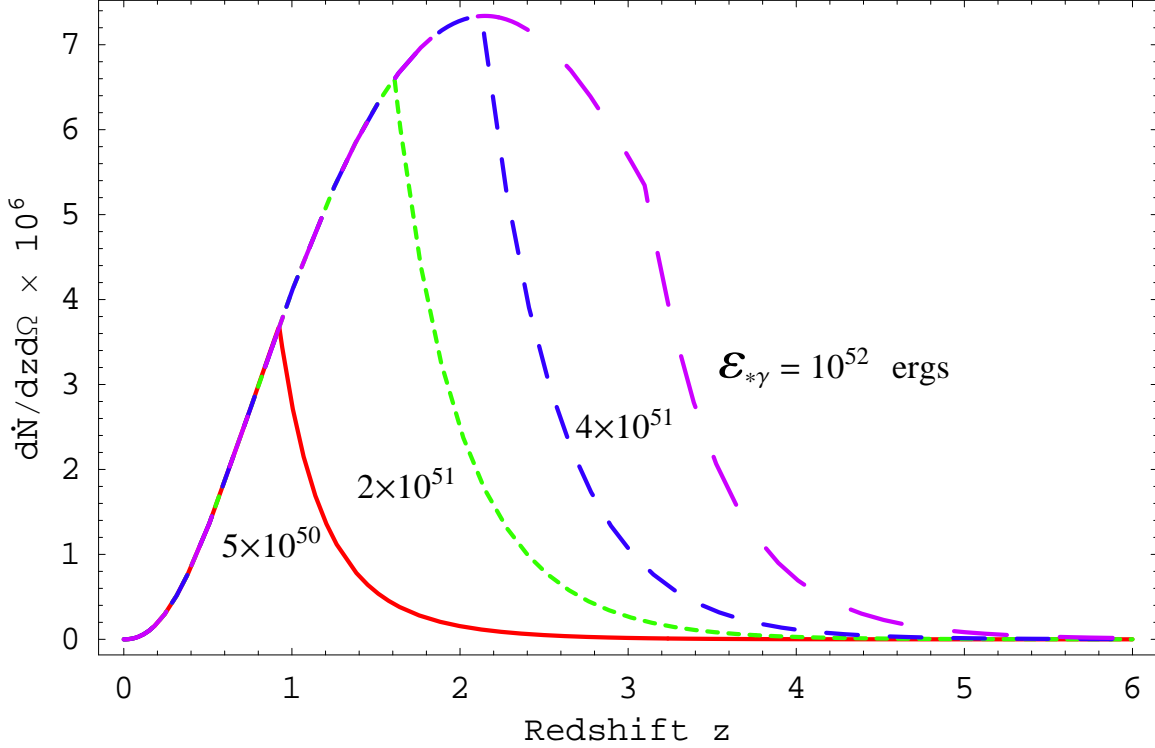


Fig. 8. Directional event rate per unit redshift [one event per $(10^{28} \text{ cm})^3$ per day per sr per z] with $\theta_{\text{min}} = 0.05 \text{ rad}$ and $\theta_{\text{max}} = 0.7 \text{ rad}$ for $E = 5 \times 10^{50}, 3 \times 10^{51},$ and 10^{52} ergs , using SFR 3.

angle samples. It is important, however, that the best t value is not too far from the mean value in order for our model to be in accord with observations. Later in the analysis we will show that our best t corrected γ -ray energy E is indeed only a factor of 2 larger than the mean.

In Figures 9, 10 and 11, we plot the calculated redshift distribution at three different corrected total γ -ray energies, $E = 2 \times 10^{51}, 5 \times 10^{51},$ and 10^{52} ergs , respectively. In each panel, each curve represents the calculated cumulative redshift distribution for the power-law index s of the jet opening angle distribution. The values $s = 0.6, 1.2, 1.8,$ and 2.4 are plotted, from far left to far right, respectively. In each figure, from top to bottom, we have $\theta_{\text{min}} = 0.05$ and $\theta_{\text{max}} = 2 \text{ radians}$, $\theta_{\text{min}} = 0.05$ and $\theta_{\text{max}} = 0.7 \text{ radians}$, and $\theta_{\text{min}} = 0.05$ and $\theta_{\text{max}} = 0.4 \text{ radians}$, respectively, as the jet opening angles. The cumulative redshift distribution (bold solid curves) of the Swift and pre-Swift samples are plotted for comparison. We do not plot $s < 2.4$, since there is little variation in the redshift distribution (see Fig. 7). The results in Figures 9, 10, and 11 clearly show that the redshift distributions for different values of s from the model do not fit the Swift redshift sample. Furthermore, the fits to both the Swift and pre-Swift samples do not correlate together with the associated range of the jet opening angle. In fact it indicates that we need larger burst rates at higher redshifts ($z > 3$). These results rule out the lower SFR, SFR 2, as can be seen in Figure 12.

The comparisons also rule out the possibility that the upper SFR explain the GRB data, even though SFR 4 has a higher SFR than SFR 2 at large redshifts. In Figure 13 we fit the Swift redshift sample using three different γ -ray energies, namely $E = 5 \times 10^{50}$, 2×10^{51} , and 10^{52} ergs, with $s = 0.6$, 1.2 , 1.8 , and 2.4 using SFR 4. The results for the range of the jet opening angle $j_{\text{min}} = 0.05$, and $j_{\text{max}} = 0.7$ radians show that the calculated redshift distribution between Swift and pre-Swift are anticorrelated, that is, smaller values of s , which would improve the fit for Swift GRBs, makes the fit for pre-Swift GRBs worse. However, with $s = 0.6$ and $E = 10^{52}$ ergs (bottom panel), the redshift distributions are marginally acceptable by the model, noting that the Kolmogorov-Smirnov one-sided test statistic for a sample of 41 and 31 GRBs at the 10% level are 0.167 and 0.187, respectively (that is, only 10% of randomly chosen samples should exhibit maximum vertical deviations from the model cumulative distribution; if it is greater than these values, then the model is an inadequate representation of the data at the 90% confidence level). Only 2.5% of randomly chosen samples should have vertical excursions greater than 0.212 and 0.238 for a sample of 41 and 31 GRBs, respectively.

When we calculate the opening angle distribution to fit the pre-Swift opening angle sample in Figure 14, however, the fit is adequate for $E = 10^{52}$ ergs and $s = 1.2$ but not for $s = 0.6$. Hence, the upper SFR (SFR 4) is statistically eliminated. Nevertheless, the results in Figure 13 suggest that a greater GRB burst rate at larger redshifts is required to fit the redshift distributions. The cumulative jet opening angle distribution (bold solid curves) of the pre-Swift sample is plotted for comparison, but not for Swift, since the available opening angles for the associated Swift redshift sample are lacking.

As a result, we consider a GRB comoving source rate density that exhibits positive evolution above redshift $z > 3$. We therefore modify the Hopkins & Beacom SFR (SFR 3) to obtain the comoving rate-density that attains (1) a constant comoving rate-density at high redshift z (SFR 5), and (2) a monotonically increasing comoving rate-density with increasing redshift (SFR 6) in order to provide a high GRB burst rate at large z (see caption to Figure 4 for coefficients of the SFR models).

In Figures 15 and 16 we begin to see some improvement in fitting the pre-Swift and Swift redshift samples when using SFR 5 and SFR 6 with $E = 2 \times 10^{51}$ ergs. Nevertheless, the fitting is still somewhat inconsistent between the pre-Swift redshift distribution and the jet opening angle. For example, in Figure 15 using SFR 5, the fitting to the pre-Swift and Swift redshift distribution shows a good fit with $s = 1.2$ for a range of jet opening angles between $j_{\text{min}} = 0.05$ and $j_{\text{max}} = 0.4$ radians (two bottom panels). However, the result from the fitting between the pre-Swift redshift distribution and the opening angle distribution with $s = 1.2$ is inconsistent (see Figures 15 and 16). Above redshift $z > 2$, the calculated redshift distribution underestimates the fractional number of bursts that should occur at high redshifts z . On the other hand, the calculated opening angle distribution overestimates the fractional number of GRBs that should occur at small opening angles. Recall that if a burst occurs at a small opening angle, then this translates into the possibility of observing this particular burst at a high redshift z . Hence, the fit with the range of

the jet opening angle $j_{\text{in}} = 0.05$, and $j_{\text{in}} = 0.4$ radians is not yet acceptable.

In Figures 17 and 18 we see similar results when using SFR 6. However, it is interesting to note that we can resolve this problem if we could increase the fractional number of GRBs at both high and low redshifts z . As a result, this will provide a self-consistent fitting between the pre-Swift redshift and the jet opening angle distributions, as well as the Swift redshift distribution. This problem can be solved by adjusting the γ -ray energy E . Using $E = 4 \times 10^{51}$ ergs, Figures 19 and 20, and Figures 21 and 22 show a statistically acceptable fit to the pre-Swift and Swift redshift distribution and the pre-Swift opening angle distribution with $s = 1.2$, and the range of the jet opening angle $j_{\text{in}} = 0.05$ and $j_{\text{in}} = 0.7$ radians for SFR 5 and SFR 6, respectively. For SFR 5, the fitting can be improved with $s = 1.3$, as indicated by the solid curves (see Figures 19 and 20).

The above analyses show that $E = 4 \times 10^{51}$ ergs gives the best fit to the pre-Swift redshift and the jet opening angle samples, and the Swift redshift sample. This best-fit γ -ray energy is interesting since Frailey et al. (2001) and Bloom et al. (2003) show that the standard-energy reservoir is $E = 10^{51}$ ergs. However, with a larger sample set, the data from Friedman & Bloom (2005) shows that E is broadly distributed between $E = 10^{51.52}$ ergs, as shown in Figure 1. Because we have been able to obtain an acceptable fit to the data with discrete values of E and t , a more complicated model where a range of values of E and t were allowed would certainly permit excellent fits to the data.

We can utilize our best-fit parameters to estimate the average beaming factor $\langle f_b^{-1} \rangle$. The beaming factor average over the opening angle distribution is given by

$$\langle f_b \rangle = \frac{\int_{j_{\text{in}}}^{j_{\text{in}}} (1 - j) g(j) d_j}{\int_{j_{\text{in}}}^{j_{\text{in}}} g(j) d_j} = \frac{1+s}{2+s} \frac{(1 - j_{\text{in}})^{2+s}}{(1 - j_{\text{in}})^{1+s}} \frac{(1 - j_{\text{in}})^{2+s}}{(1 - j_{\text{in}})^{1+s}} ; \quad (21)$$

where $g(j)$ is given in equation (12). Using the best-fit parameters $s = 1.2$ and $s = 1.3$ and the range of the jet opening angles between $j_{\text{in}} = 0.05$ and $j_{\text{in}} = 0.7$, we obtain $\langle f_b \rangle^{-1} = 34 - 42$ as the beaming factor for $s = 1.2$ and $s = 1.3$, respectively. Our value of $\langle f_b \rangle^{-1}$ is about a factor of 2 smaller than the value obtained by Guetta, Piran, & Waxman (2005).

We can also infer the luminosity function from the jet opening angle distribution. From equations (8) and (9), the jet opening angle distribution is $dN = d_j = g(j)$, which is related to luminosity by the expression

$$\frac{dN}{dL} = g(j) \frac{d_j}{dL} ; \quad (22)$$

where L is the GRB apparent isotropic luminosity, and $g(j)$ is the jet opening angle distribution given in equation (12). Since the energy flux is defined as $E = L = 4 d_L^2$ or $f = F = L = 4 d_L^2$, then the isotropic luminosity in the bursting frame is $L = L$, so that $L = 4 d_L^2 f$. Utilizing equation (17), the jet opening angle in terms of isotropic luminosity is given by

$$j = 1 - \frac{E}{t b L} : \quad (23)$$

Substituting equation (23) into equation (22), we obtain $dN = dL / L^{(s+2)}$ after utilizing the jet opening angle distribution in equation (12). Since our best fit to the pre-Swift redshift and opening angle samples and the Swift redshift sample constrains the jet opening angle distribution power-law index s between 1.3 and 1.2 for using SFR 5 and SFR 6, respectively, our apparent isotropic luminosity function is $\propto L^{-3.25}$ within the uniform jet model. For our best fitting model with jet opening angles ranging from $j = 0.05$ to $j = 0.7$ rad, this implies bolometric γ -ray luminosities in the range 2×10^{41} to 3×10^{43} ergs s^{-1} . In the universal structured jet model, the luminosity function is suggested to be $\propto L^{-2}$ (e.g., Guetta, Piran, & Waxman 2005; Perna, Sari, & Frail 2003); others have suggested that the luminosity function is $\propto L^{-2.3}$ (e.g., Lloyd-Ronning, Fryer, & Ramirez-Ruiz 2002).

The results for our best fitting model are shown in Figure 23. The fraction of high-redshift GRBs in the high-redshift universe implied by our fits using SFR 5 and SFR 6 is estimated at 8 { 12% and 2.5 { 6% at $z = 5$ and $z = 7$, respectively. If this fraction is not observed with Swift, then it suggests that SFR 5 and SFR 6 do not continue with positive evolution $z > 5$. Indeed, it is likely that the formation rate of GRBs at high redshift declines at sufficiently high redshift. We can also derive the fractional number of GRBs with $z > 0.25$ from Figure 23. We find that $\sim 0.2\%$ of long duration GRBs should occur in the low-redshift ($z > 0.25$) universe.

4. DISCUSSION AND CONCLUSIONS

In this work, we considered whether the differences between the pre-Swift and Swift redshift distributions can be explained with a physical model for GRBs that takes into account the different flux thresholds of GRB detectors. The model presented here parameterizes the jet opening angle distribution for an assumed F spectrum, and finds best fit values for the γ -ray energy release for different functional forms of the comoving rate density of GRBs, assuming that the properties of GRBs do not change with time. Adopting the uniform jet model, we assumed that the energy per solid angle is roughly constant within a well-defined jet opening angle. The pre-Swift redshift sample suggests that the range of the jet opening angle is between 0.05 and 0.7 radians. We explored three different ranges of jet opening angle with $j_{\min} = 0.05$, and $j_{\max} = 0.2, 0.7$, and 0.4 radians.

The results in χ^2 show that an intrinsic distribution in the jet opening angles and single values for all other parameters yields a good fit to the pre-Swift and Swift redshift samples, and furthermore provides an acceptable fit to the distribution of opening angles measured with pre-Swift GRB detectors. A good fit was only possible, however, by modifying the Hopkins & Beacom SFR to provide positive evolution of the SFR history of GRBs to high redshifts (SFR 5 and SFR 6; see Fig. 4). The best fit values were obtained with $E_{\gamma} = 4 \times 10^{41}$ ergs, $j_{\min} = 0.05$, $j_{\max} = 0.7$ radians, and $s = 1.25$. The best-fit value for the absolute γ -ray energy released by a GRB is about a factor of 2 larger than the mean value of the Friedman & Bloom (2005) sample of pre-Swift GRBs.

The results of our fitting therefore indicate that GRB activity was greater in the past and is

not simply proportional to the bulk of the star formation as traced by the blue and UV luminosity density of the universe. This result agrees with the conclusions of the study by Daigne et al. (2006), who also note that the star formation rate cannot increase in proportion to greater past GRB activity, as this would result in overproduction of metals. Changes in the progenitor population or GRB properties, for example, due to changing metallicities with time, might account for the large number of high-redshift GRBs observed with Swift, but this would introduce a large number of unconstrained parameters. Moreover, one would then have to explain why the Amati and Hirlanda correlations relating spectral properties and energy releases are insensitive to redshift.

Assuming that the GRB properties do not change with time, we therefore find that the GRB source rate density must display positive evolution to at least $z \approx 5$. Why would GRB activity be greater in the past? One possibility suggested by recent studies (Stanek et al. 2006; Fruchter et al. 2006) on the metallicities of host galaxies of GRBs is that GRBs derive from progenitor stars with a lower metallicity than the progenitors of Type II SNe. In this case, one might expect that the peak of GRB activity would occur earlier in the universe than during the peak of star formation activity at $z \approx 2 \{ 3$. The high-redshift fraction of GRBs detected with Swift will test the validity of SFR 5 and SFR 6 used to model the GRB data.

The models that fit the data imply that 8 { 12% of Swift GRBs occur at $z \approx 5$, in accord with the data as shown in Figure 23. Our model predicts that 2.5 { 6% of GRBs should be detected from $z = 7$. If no GRB with $z > 7$ is detected by the time ≈ 100 Swift GRBs with measured redshifts are found, then we may conclude that the GRB formation rate has begun to decline above $z = 5$. By contrast, if a few $z \approx 7$ GRBs have been detected within the next year or two with Swift, then this would be in accord with our model and would support the conjecture of Bromm & Loeb (2006) that a second episode of Population I and II star formation took place at $z \approx 5$, possibly even including some GRBs that originate from Population III stars. Our model parameters suggest that GRBs can be detected with Swift to a maximum redshift $z = 20$, even given the limits placed on the range of jet angles, in particular, $\tan \theta \approx 0.05$.

The relationship between the galaxies that host GRBs and their metallicities remains controversial, with evidence for high-redshift, low-metallicity GRB host galaxies (Fruchter et al. 2006) countered by examples of GRBs found in galaxies with moderate metallicity (Berger et al. 2006; Fynbo et al. 2006). Stanek et al. (2006) find that 5 GRBs, or several per cent of the GRB population with known redshifts, are found at low ($z < 0.25$) redshift in galaxies that have very low metallicity compared with Solar metallicity and with the distribution of metallicities of low-redshift galaxies in the Sloan Digital Sky Survey. In 4 out of the 5 low- z GRBs, the apparent isotropic energy release of these GRBs is much smaller than 10^{51} ergs, and so these GRBs are unrepresentative of typical long duration GRBs. Moreover, the large number of these low redshift GRBs already means that they are not typical of the sample of GRBs considered in this paper, as the model prediction is that $\approx 0.14 \{ 0.2\%$ of the "classical" GRBs should be detected at low redshifts.⁴

⁴A value of $\approx 0.3\%$ can be estimated by considering the fractional volume within $z = 0.25$ compared with $z = 1$,

These low-redshift GRBs may also belong to a completely distinct population of GRBs compared to their high-redshift counterparts, as also suggested by the differing luminosity functions of the two populations (Liang et al. 2006). Alternatively, the low-redshift GRBs could be normal GRBs that appear weak because, for example, their jetted emission is observed off-axis (e.g. Yamazaki et al. 2003).

Figure 24a shows the model integral size distribution (see eq. [18]) of GRBs predicted by our best model. The plots are normalized to the current total number of observed GRBs per year from BATSE, which is 550 bursts per 4 sr exceeding a peak flux of 0.3 photons cm⁻² s⁻¹ in the E = 50–300 keV band for the t = 1.024 s trigger time (Band 2002). From the model size distribution, we find that 340 to 360 GRBs per year should be detected with a BATSE-type detector over the full sky above an energy flux threshold of 10⁷ ergs cm⁻² s⁻¹, or photon number threshold of 0.625 ph cm⁻² s⁻¹. This range of values is determined by the two models to within SFR 6 and SFR 5, respectively. We estimate from our fits that 1190 { 1370 GRBs take place per year per 4 sr with a flux & 10⁸ ergs cm⁻² s⁻¹, or 0.625 ph cm⁻² s⁻¹. The field of view of the BAT instrument on Swift is 1.4 sr (Gehrels et al. 2004), implying that Swift should detect 130 { 150 GRBs per year; currently, Swift observes about 100 GRBs per year. This minor discrepancy may be a consequence of using a flat GRB spectrum in our model.

We also show the differential size distribution of BATSE GRBs from the Fourth BATSE catalog (Paciesas et al. 1999) in comparison with our model prediction in Figure 24b. As can be seen, our model gives a good representation of the size distribution of the BATSE GRB distribution within the statistical error bars, except for a slight overprediction of the number of the brightest GRBs (see also Daigne et al. 2006; Bottcher & Dermier 2000). These brightest GRBs typically originate from z > 1, possibly suggesting a slight reduction in the number of GRBs with z > 1 compared to the GRB rate densities considered. Below a photon number threshold of 0.3 ph cm⁻² s⁻¹ in the 50–300 keV band, the observed number of GRBs falls rapidly due to the sharp decline in the BATSE trigger efficiency at these photon fluxes (see Paciesas et al. 1999). The size distribution of the Swift GRBs will extend to much lower values, 0.0625 ph cm⁻² s⁻¹, and we can use our model to predict the peak flux size distribution to fit the Swift data, noting however that the Swift triggering criteria are more complicated than a simple rate trigger, particularly near threshold (Band 2006).

We can derive the burst rate in our local universe by normalizing our best models to the BATSE results of 340 { 360 GRBs per year full sky with peak fluxes exceeding 10⁷ ergs cm⁻² s⁻¹. Comparing this value with the rate calculated from eq. (18) for our best models, we obtain local GRB rate densities of $n_{GRB} = 9.6 \text{ G pc}^{-3} \text{ yr}^{-1}$ for SFR 5 and $n_{GRB} = 7.5 \text{ G pc}^{-3} \text{ yr}^{-1}$ for SFR 6. Since the mean volume occupied by an L₁ galaxy in the local universe is 200 M pc³ (Loveday et al. 1992; Wijers et al. 1998), we obtain the local event rate in our Galaxy, assumed to be a typical L₁ galaxy, to be $\sim 1.9 \cdot 10^6$ and $1.5 \cdot 10^6$ events per year per L₁ galaxy, for SFR 5 and SFR 6, respectively. This implies that about 1 event occurs every 0.6 M yrs in our Galaxy. Comparing

and that the SFR activity at z = 1 was a factor = 5 greater than at z < 0.25.

this to the rate of Type Ib/c supernovae of 1 every 360 years in our Galaxy (Cappellaro et al. 1999), we estimate that the rate of GRBs is only 0.06% of the rate of SN Ib/c supernovae in the Galaxy. Berger et al. (2003) find that 3% of GRBs could originate from SN Ib/c by comparing the radio brightnesses of SN Ib/c with that of SN 1998bw associated with GRB 980425. Our results fall comfortably within the observational limits. We also find that about 1 out of every 20,000 SNe make a GRB, compared to the value of 1 out of every 10^5 to 10^6 found by Daigne et al. (2006).

If GRBs do occur at the rate of more than once per Myr in the Milky Way, depending on uncertain metallicity effects (Stanek et al. 2006), then the Earth will intercept the beam of a GRB about once every 25 Myrs, given the beaming factor $h_f^{-1} \approx 40$ obtained in our analysis. If a Milky Way GRB is located at an average distance of 10 kpc, then the average fluence deposited by the GRB is on the order of 10^7 ergs cm $^{-2}$. Strong astrobiological effects begin to be important when the GRB fluence is 10^8 to 10^9 ergs cm $^{-2}$, or when the GRB occurs within 1 to 2 kpc with its beam pointing in our direction (Demmer & Holm 2005). This will happen perhaps a few times per Gyr, so that GRBs could have significant effects on terrestrial evolution (Mellott et al. 2004; Thomas et al. 2005).

The number of jet opening angles measured with follow-up observations of Swift GRBs is not yet sufficient to produce a statistically reliable sample. Thus our jet opening angle distribution shown in Figures 20 and 22 with $s = 1.3$ and 1.2 , for SFR 5 and SFR 6, respectively, provide a prediction for Swift. With Swift and pre-Swift thresholds of 10^8 and 10^7 ergs cm $^{-2}$ s $^{-1}$, our model predicts the mean measured jet opening angle $h_{ji} = 0.16$, and 0.12 rad, respectively, which can be compared with the measured average value of $h_{ji} = 0.125$ for the pre-Swift sample. Thus we expect to detect more faint low-redshift, large opening angle GRBs that pre-Swift satellites could not detect (see also Perna, Sari, & Frail 2003). It is interesting to note that with a better detector sensitivity, the mean jet angle is shifted to a higher angle and not vice versa, as might be expected. This suggests that on average we expect to see more long-duration bursts with larger opening angle ($j > 0.12$ radian), meaning that the mean times for the achromatic breaks in the light curves could be longer than for the pre-Swift GRBs when one also takes into account the larger mean redshift of the Swift sample.

In conclusion, we have developed a physical model for GRBs and obtained parameters to the model by fitting the GRB redshift and opening angle distributions. We could only obtain statistically acceptable joint fits if the comoving rate density of GRBs increases monotonically to $z = 5$. Our fitting results give a rate of 1 GRB every 600,000 yrs in our Galaxy if metallicity effects do not play a large role in the galaxies in which GRBs are formed. In this case, the increase in the GRB rate density to high redshifts would have a different cause, for example, an episode of enhanced star formation at $z = 5$ (Bromm & Loeb 2006). The opening angle distribution of GRBs measured with Swift, and the fraction of low- z and high- z standard long-duration GRBs will test this model.

correspondence. T . L . is funded through NASA GLAST Science Investigation No. D P R -S-1563-Y and a Swift Guest Investigator Grant No. NNG 05ED411. The work of C . D . D . is supported by the Office of Naval Research.

A P P E N D I X

A . Bursting Rate of Beam ed Cosm ic Sources in a Flat CDM Universe

The Robertson-Walker metric

$$ds^2 = c^2 dt^2 - R^2(t) \frac{dr^2}{1 - kr^2} + r^2 d\Omega^2; \quad (A 1)$$

is written for suitable comoving radial coordinates r in terms of a dimensionless scale factor $R(t)$. For a flat universe, $k = 0$, and for a closed and open universe, $k = +1$ and $k = -1$, respectively. If the scale factor $R(t) = R = 1$ is set equal to unity at the present epoch, then the following relations hold from the definition

$$z = \frac{r_{\text{obs}} - r_{\text{em}}}{r_{\text{em}}} = -1;$$

namely

$$1 + z = \frac{R}{r} = - = \frac{t}{t} = -; \quad (A 2)$$

where the last expression applies to photons and relativistic particles in an expanding universe, and $R = R(t)$.

The proper volume element of a slice of the universe at time t is, from eq. (A 1),

$$dV = \frac{(R r)^2 R dr}{P \frac{1}{1 - kr^2}} = R^3 r^2 dr; \quad (A 3)$$

specializing to a flat universe. The proper time element elapsed for a photon to propagate a differential comoving distance at earlier time t is just

$$c dt = R dr;$$

Thus $dV = dA R dr = (R r)^2 dA R dr$, and $dV = dA R dr = (R r)^2 R dr = r^2 dr$, so that

$$\frac{dA}{dA} = \frac{R}{R} = \frac{2}{(1 + z)^2};$$

and

$$dA = (R r)^2 dA = dA \frac{R r}{R r}^2 = (R r)^2 = dA (1 + z)^2 (R r)^2$$

for areas referred to the same comoving coordinate. The area of the universe intercepted by our telescope is much smaller when $z \ll 1$.

The energy flux

$$\frac{dE}{dA dt} = \epsilon = \frac{L}{4 d_L^2} = \frac{dE}{4 d_L^2 dt} = (4 d_L^2)^{-1} \frac{dE}{dE} \frac{dt}{dt} \frac{dE}{dA dt} dA = \frac{(1+z)^4}{4 d_L^2} \frac{dE}{dA dt} 4 (R r)^2 ; \quad (A 4)$$

using the definition of the luminosity distance, so that

$$d_L^2 = (1+z)^2 (R r)^2 ; \quad (A 5)$$

We now introduce the GRB emissivity function $\underline{n}(z)$ (events $\text{cm}^{-3} \text{s}^{-1}$), which by its very nature is highly directional. We establish a coordinate system where the angle between the axis of the jet and the radial direction from an observer here on Earth is defined by the vector direction $\theta = (\theta; \phi) = (\arccos \theta; \phi)$. The relation between the bursting rate $\underline{n}(z)$ per unit proper volume at redshift z and the comoving GRB emissivity $\underline{n}_\infty(\theta; z)$ is just

$$\underline{n}(z) = (1+z)^3 \int d^3 \theta \underline{n}_\infty(\theta; z) ; \quad (A 6)$$

The directional event rate is

$$\frac{dN}{dV} = \frac{1}{4} \int_0^z dV \underline{n}(z) \frac{dt}{dt} ; \quad (A 7)$$

Using eqs. (A 3) and (A 5) in eq. (A 7), we therefore have

$$\frac{dN}{dV} = c \int_0^z dz \frac{d_L^2(z)}{(1+z)^2} \frac{dt}{dz} \int d^3 \theta \underline{n}_\infty(z; \theta) ; \quad (A 8)$$

For randomly oriented two-sided jets,

$$\underline{n}_\infty(\theta; z) = \frac{\underline{n}_\infty(z)}{2} ; \quad (A 9)$$

where $\underline{n}_\infty(z)$ is the z -dependent comoving rate density of GRBs.

For a flat CDM universe,

$$\frac{dz}{dt} = H_0 (1+z)^{\frac{p}{m}} \frac{1}{(1+z)^3 + \frac{p}{m}} \quad (A 10)$$

(Peebles 1993), where m and p are the ratios of the energy densities of total mass, dominated by dark matter, and dark energy, respectively, compared to the critical density. Substituting eqs. (A 10) and (A 9) into eq. (A 8) gives the result, eq. (9), for randomly oriented GRB sources.

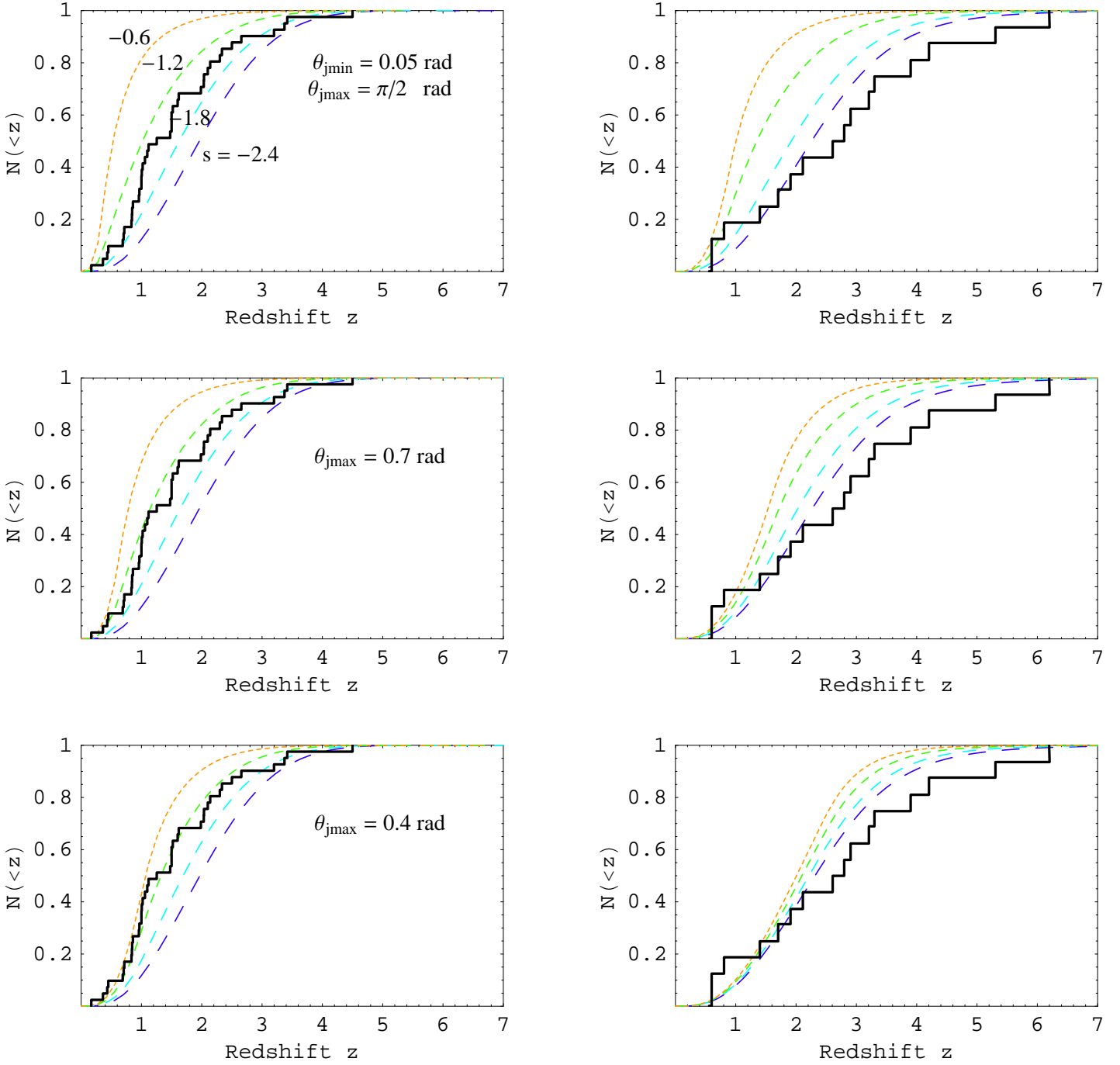


Fig. 9. Measured and model redshift distributions for SFR 3 (Hopkins & Beacom 2006). In the left column, from top to bottom, we have the pre-Swift cumulative redshift distribution with the assumed range of jet opening angles $\theta_{j\min} = 0.05$, $\theta_{j\max} = -2$, 0.7 , and 0.4 radians, respectively. The right column has results as in the left column but for Swift data. In each panel, each curve represents the cumulative redshift distribution for different jet opening angle power-law indices s , where $s = -0.6$, -1.2 , -1.8 , and -2.4 , from far left to far right, respectively. The assumed gamma-ray energy is $E = 2 \times 10^{51}$ ergs.

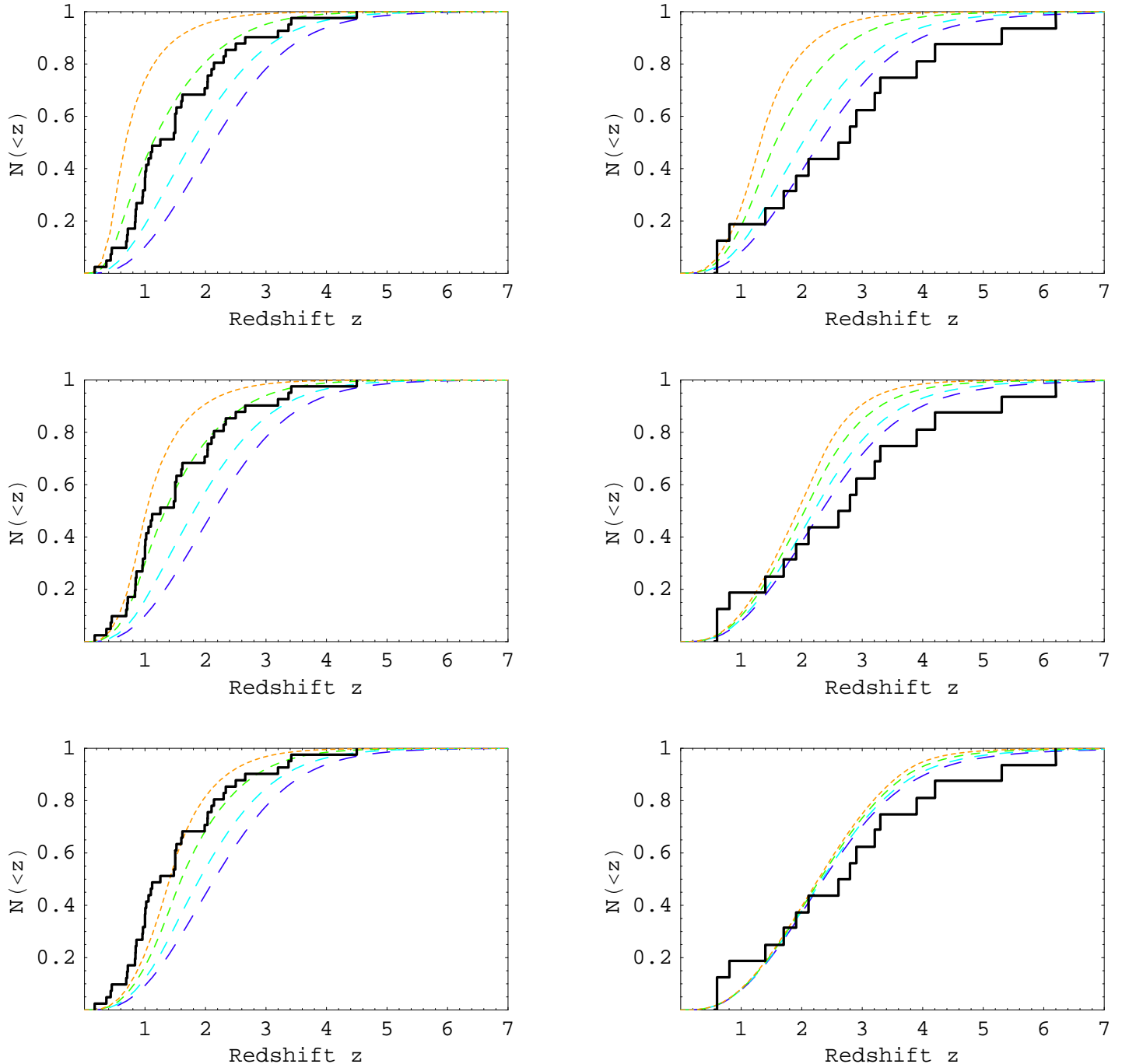


Fig. 10. | SFR 3: Same as Figure 9 but for $E = 5 \times 10^{11}$ ergs.

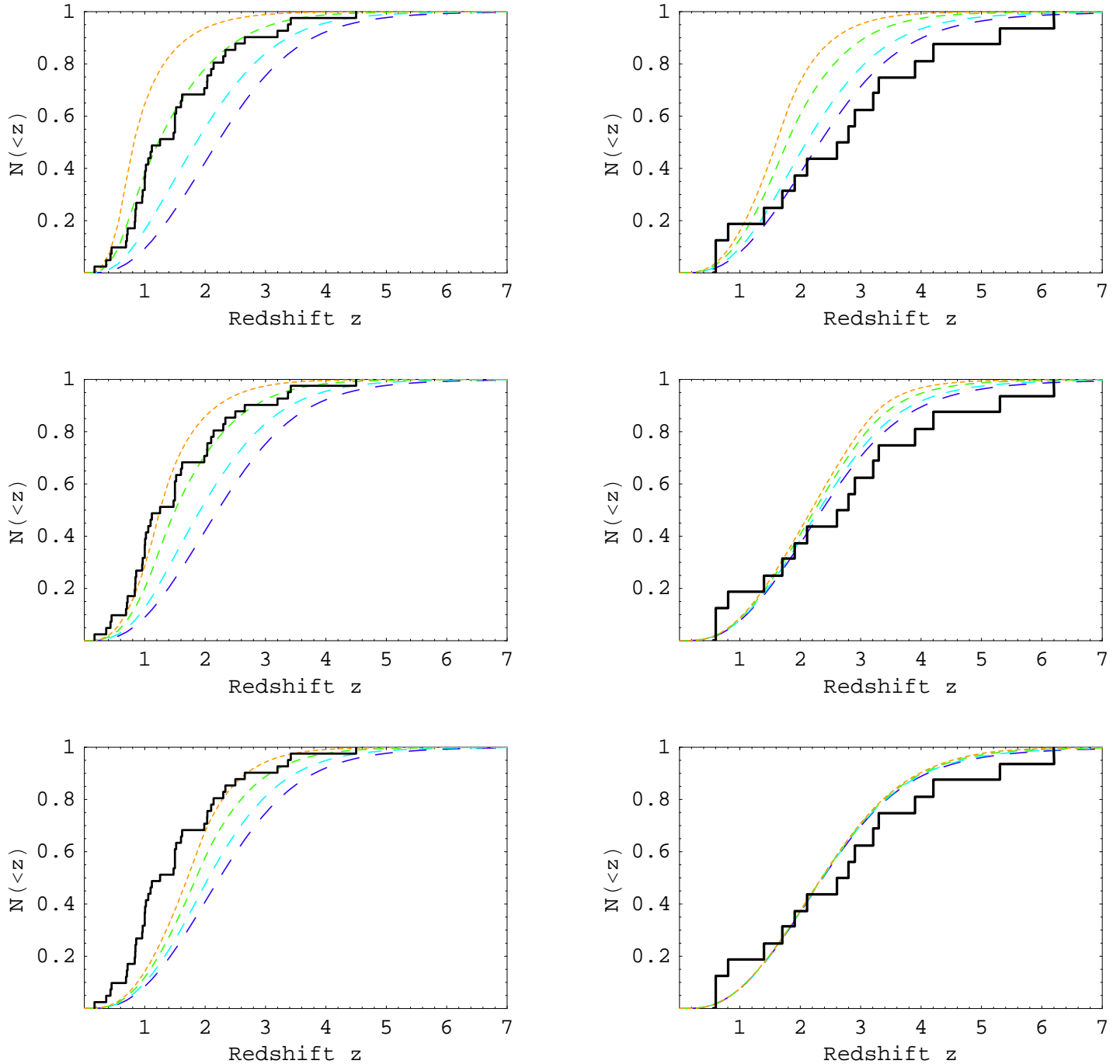


Fig. 11. | SFR 3: Same as Figure 9 but for $E = 10^{52}$ ergs.

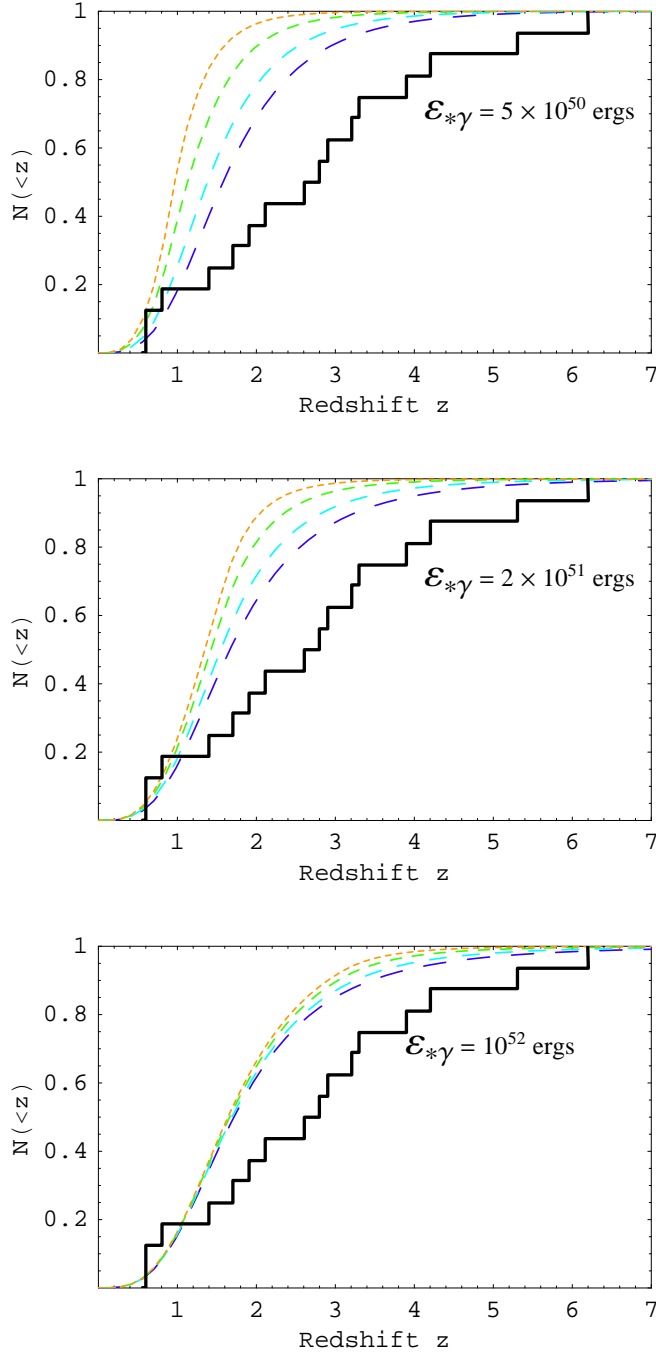


Fig. 12. | SFR 2: Cumulative redshift distribution with an assumed range of the jet opening angles $\beta_{\min} = 0.05$ and $\beta_{\max} = 0.7$ radians. From top to bottom, the assumed gamma-ray energies are 5×10^{50} , 2×10^{51} , and 10^{52} ergs, respectively. Each curve represents the cumulative redshift distribution for different power-law indices s , where $s = 0.6, 1.2, 1.8$, and 2.4 , from far left to far right, respectively.

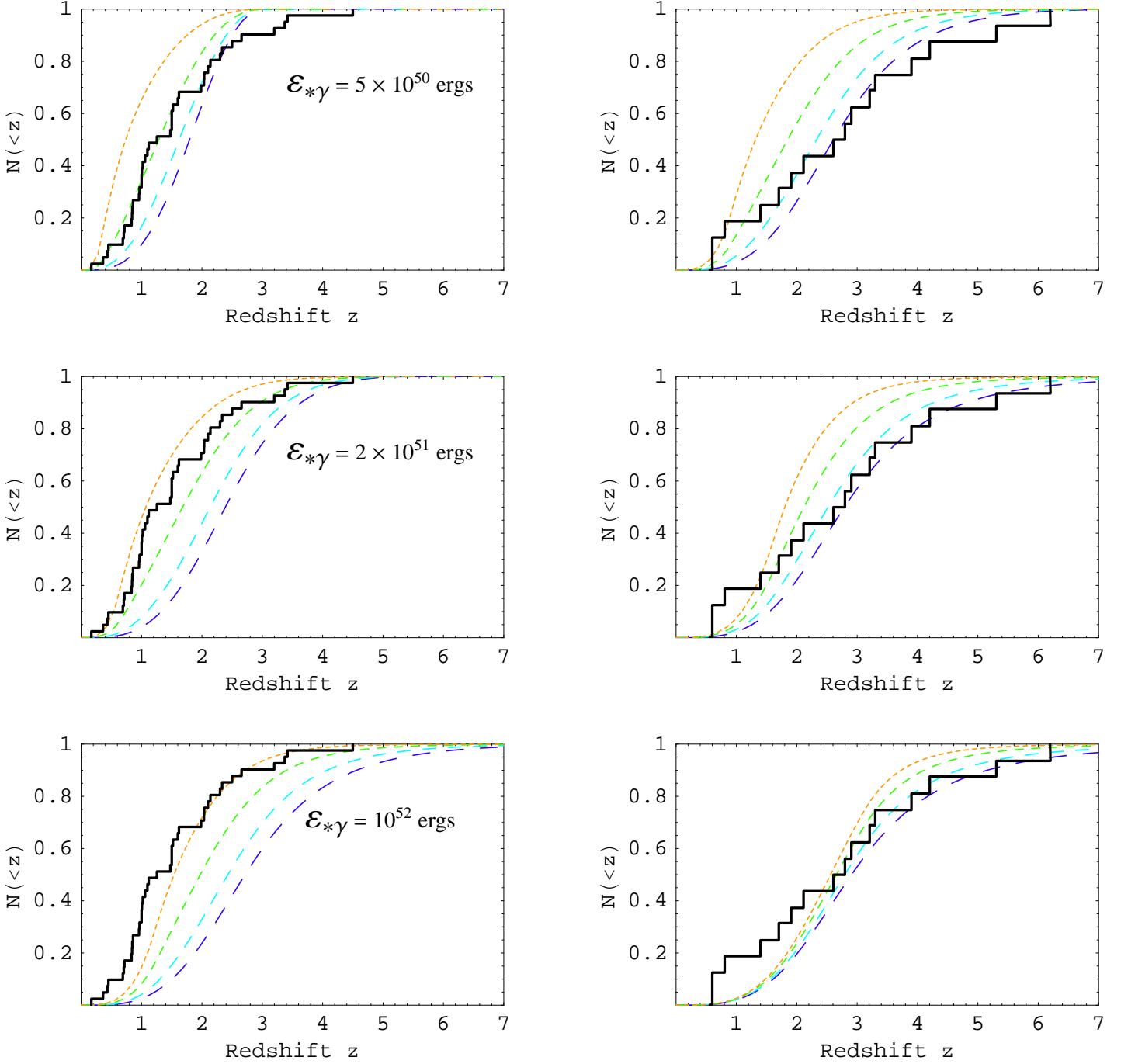


Fig. 13. | SFR 4: In the left column from top to bottom, we have the pre-Swift cumulative redshift distribution with the assumed gamma-ray energy $E_{*g} = 5 \times 10^{50}$, 2×10^{51} , and 10^{52} ergs, and an assumed range of the jet opening angles between $\gamma_{\text{in}} = 0.05$ and $\gamma_{\text{in}} = 0.7$ radians. The left and right columns show the model distributions for pre-Swift and Swift data, respectively. In each panel, each curve represents the cumulative redshift distribution for different indices s , where $s = 0.6, 1.2, 1.8$, and 2.4 , from far left to far right, respectively.

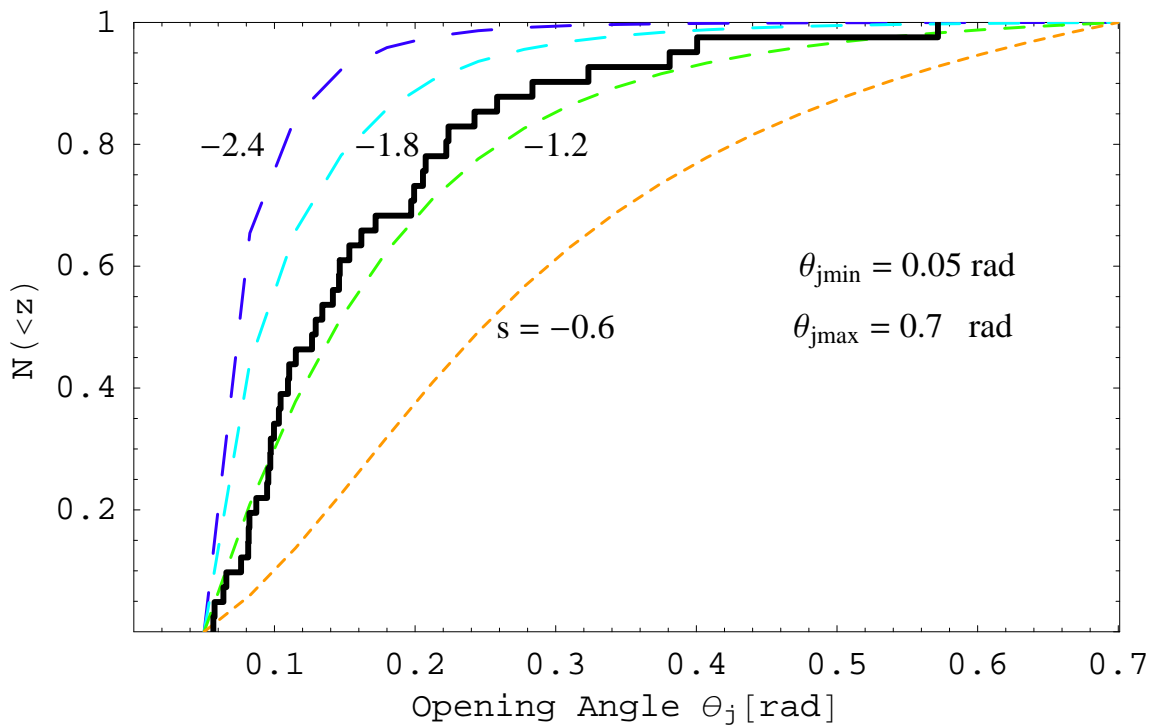


Fig. 14. | SFR 4: Cumulative opening-angle distribution with an $E = 10^{52}$ ergs, and an assumed range of the jet opening angles between $\theta_{j\min} = 0.05$ and $\theta_{j\max} = 0.7$ radians. Each curve represents the cumulative opening-angle distribution for different indices s , where $s = -0.6, -1.2, -1.8$, and -2.4 , from far right to far left, respectively.

{ 30 }

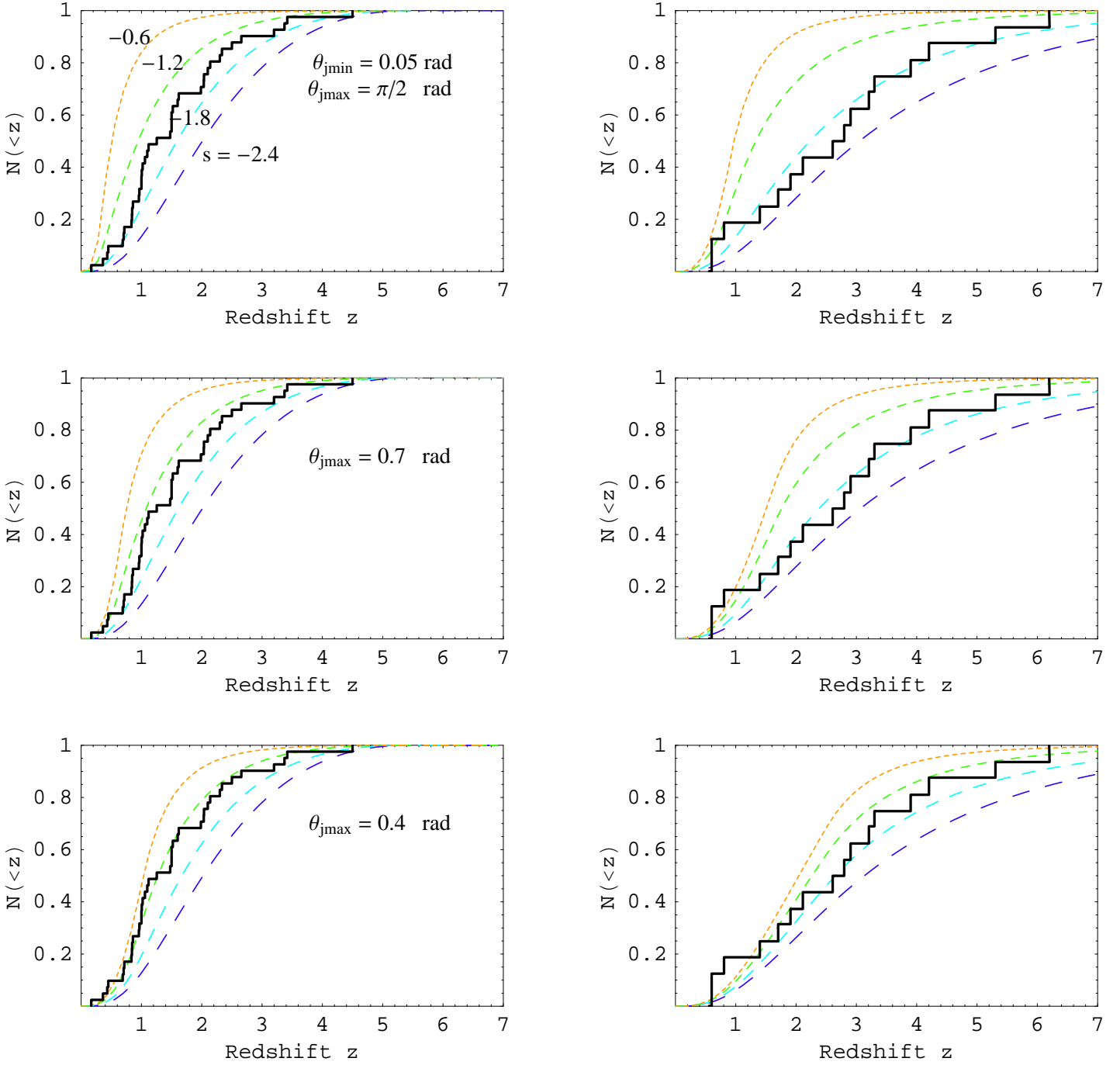


Fig. 15. | SFR 5: In the left column, from top to bottom, we have the pre-Swift cumulative redshift distribution with the jet opening angles ranging from $\theta_{j\min} = 0.05$ to $\theta_{j\max} = 0.7$, and 0.4 radians, respectively. In the right column we have the same thing as in the left column but for Swift data. In each panel, each curve represents the cumulative redshift distribution for indices s , where $s = 0.6, 1.2, 1.8$, and 2.4 , from far left to far right, respectively. The assumed gamma-ray energy is $E = 2 \times 10^{51}$ ergs.

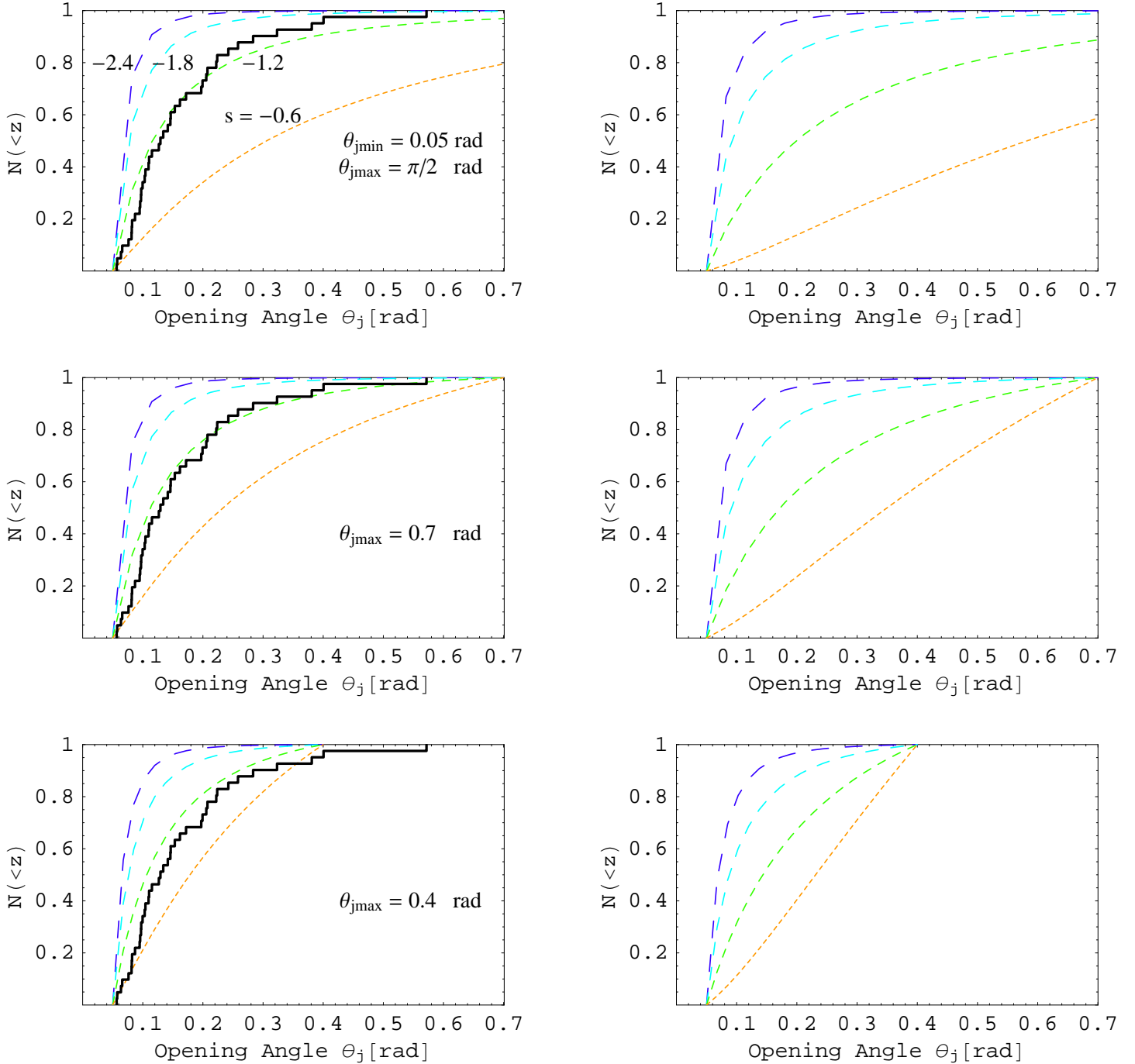


Fig. 16. | SFR 5: In the left column from top to bottom, we have the pre-Swift cumulative opening-angle distribution with the jet opening angles ranging from $\theta_{j\min} = 0.05$ to $\theta_{j\max} = 0.2, 0.4$, and 0.7 radians, respectively. In the right column we have the same thing as in the left column but for the Swift data. In each panel, each curve represents the cumulative redshift distribution for indices $s = 0.6, 1.2, 1.8$, and 2.4 , from far right to far left, respectively. The assumed gamma-ray energy is $E = 2 \times 10^{51}$ ergs.

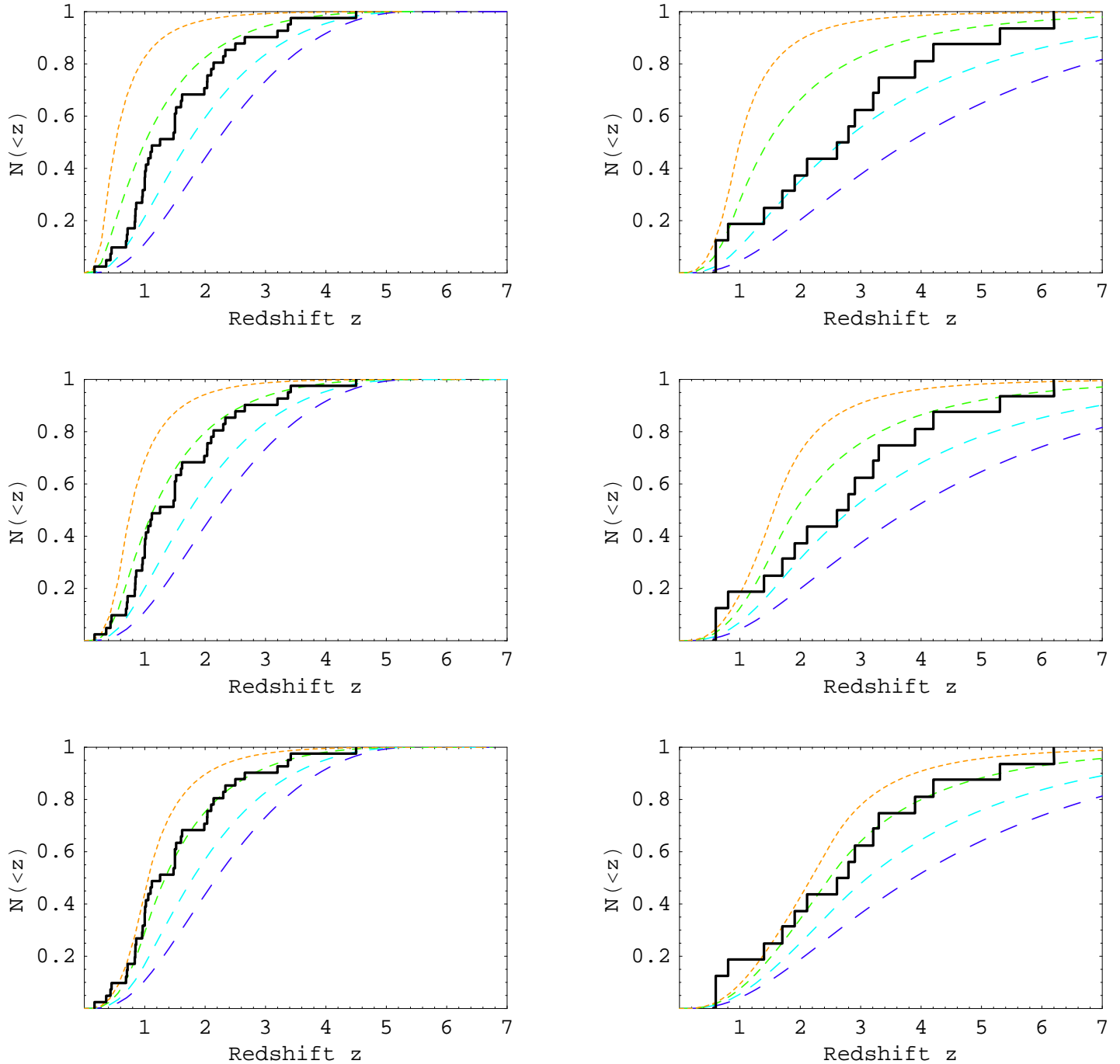


Fig. 17. | SFR 6: Same as Figure 15 with $E = 2 \times 10^{51}$ ergs.

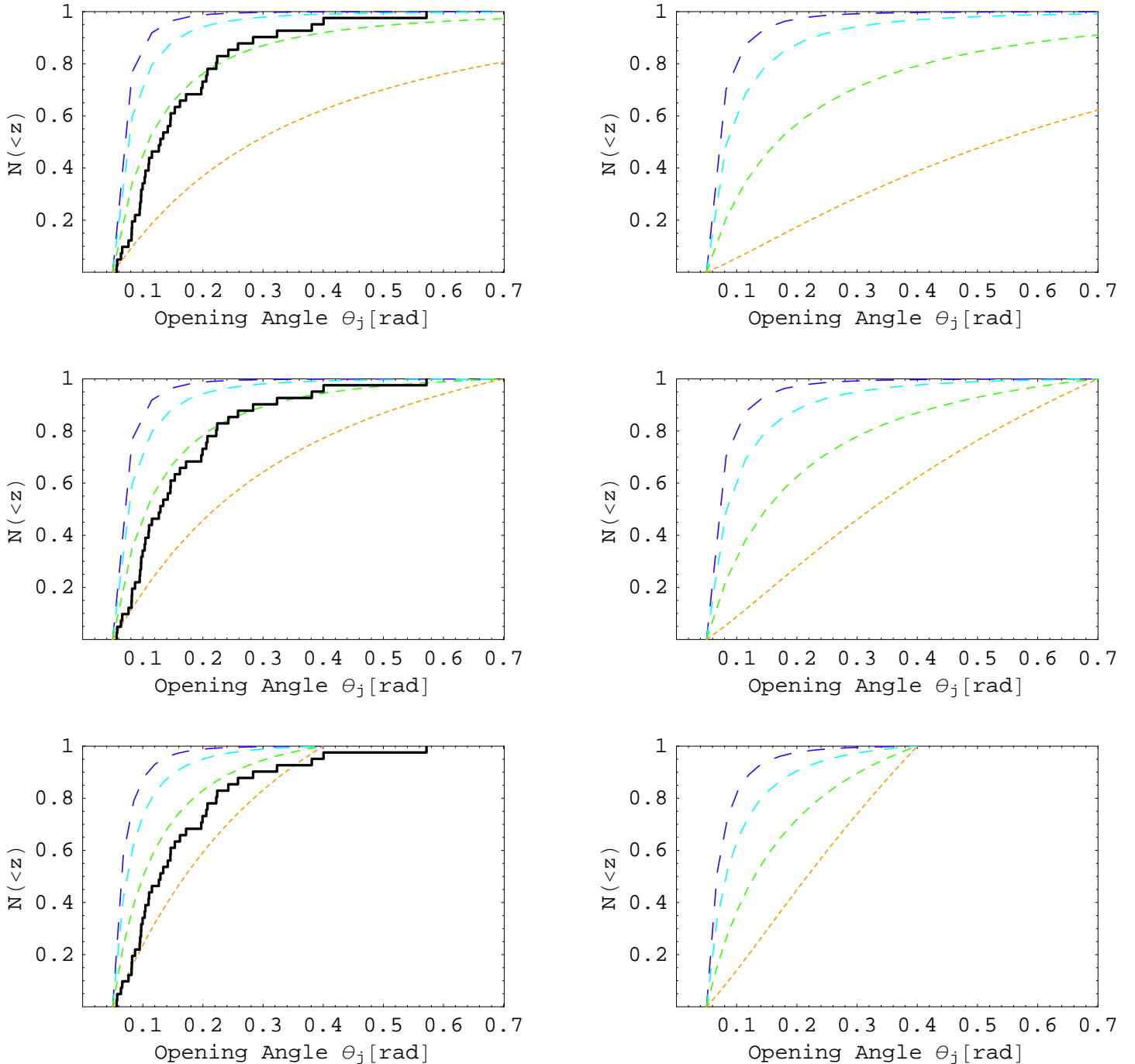


Fig. 18. | SFR 6: Same as Figure 16 with $E = 2 \times 10^{51}$ ergs.

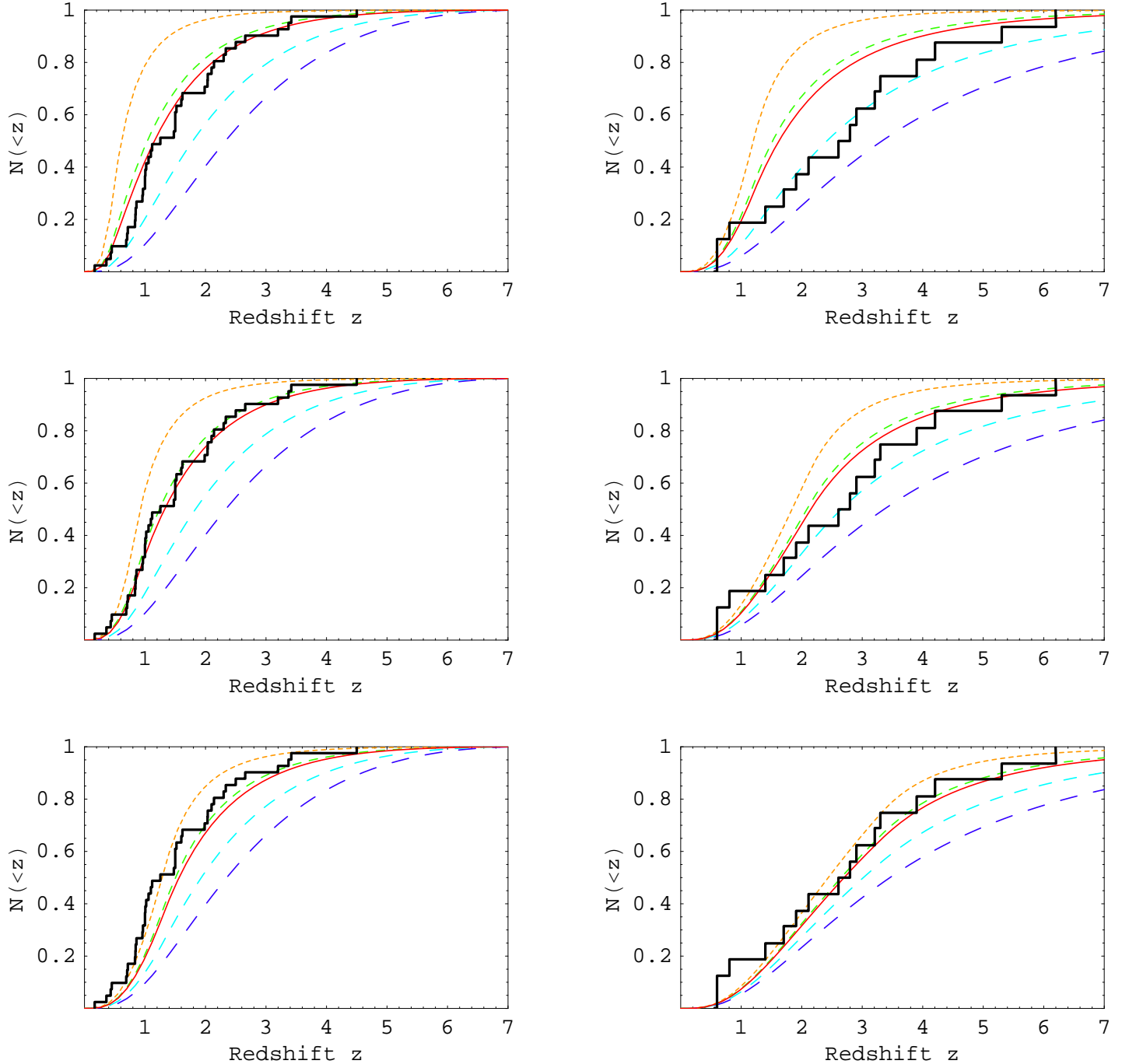


Fig. 19. | SFR 5: Same as Figure 15 with $E = 4 \times 10^{51}$ ergs. The solid curves are for $s = 1:3$.

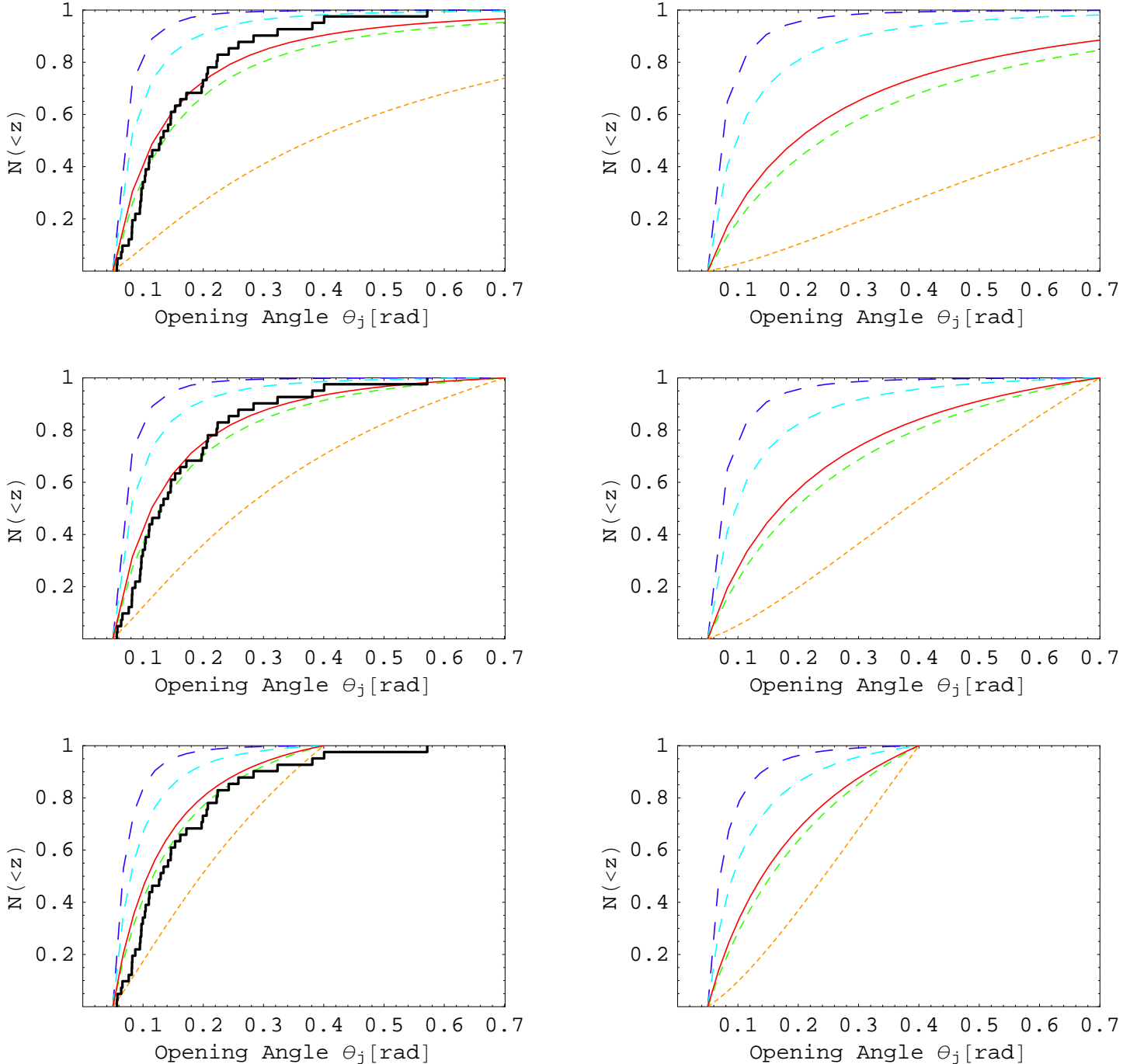


Fig. 20. | SFR 5: Same as Figure 16 with $E = 4 \times 10^{51}$ ergs. The solid curves are for $s = 1:3$.

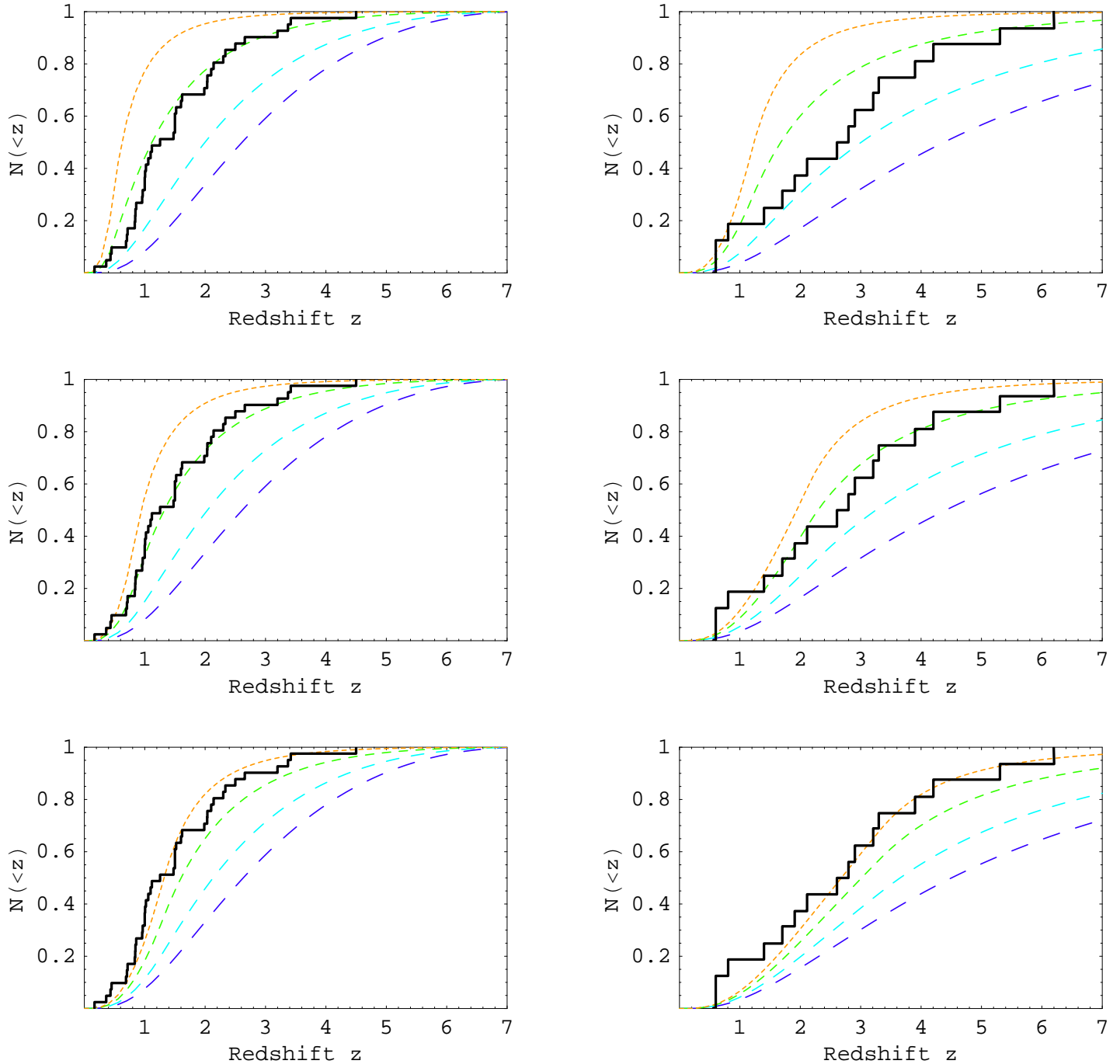


Fig. 21. | SFR 6: Same as Figure 15 with $E = 4 \times 10^{51}$ ergs.

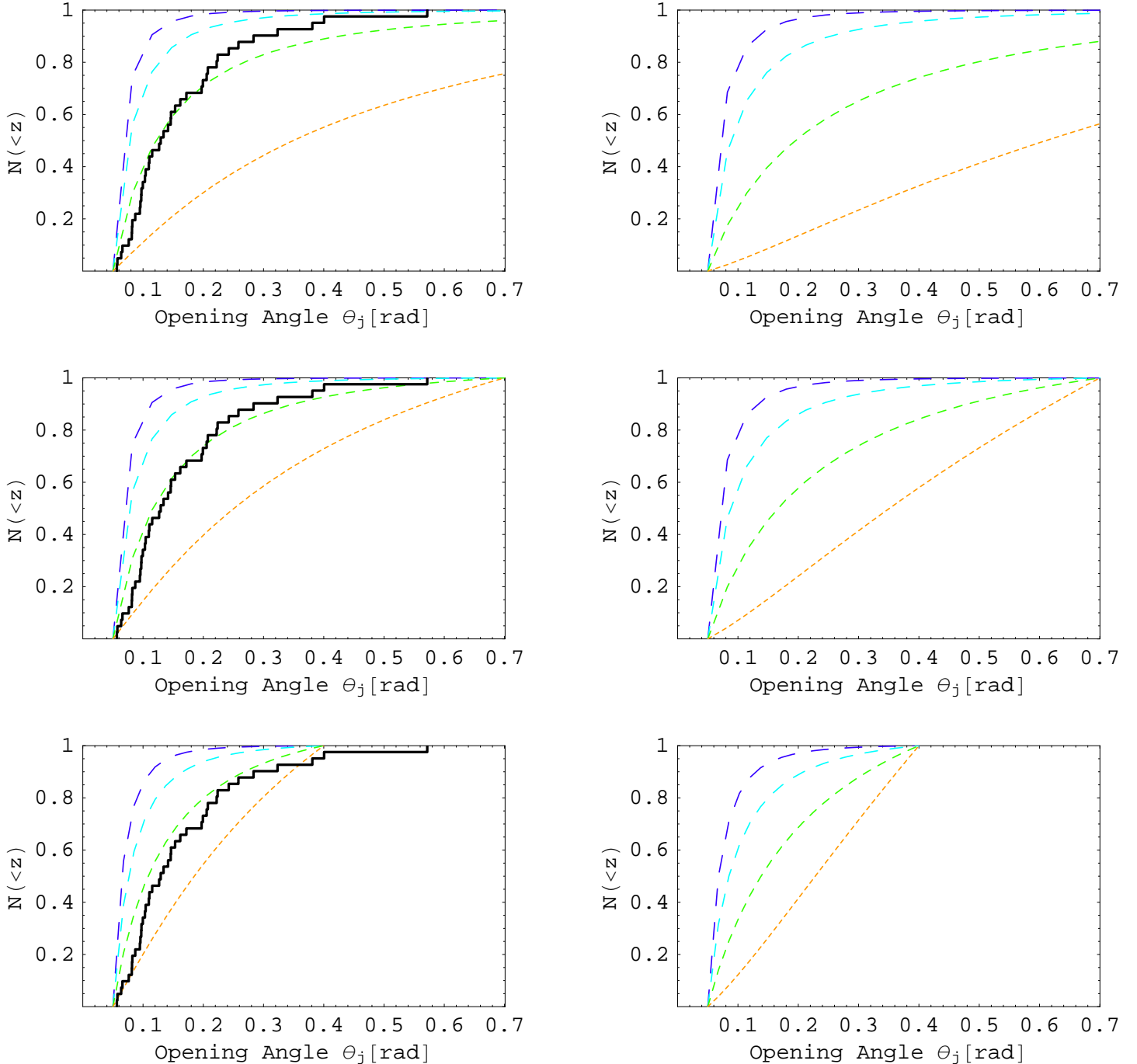


Fig. 22. | SFR 6: Same as Figure 16 with $E = 4 \times 10^{51}$ ergs.

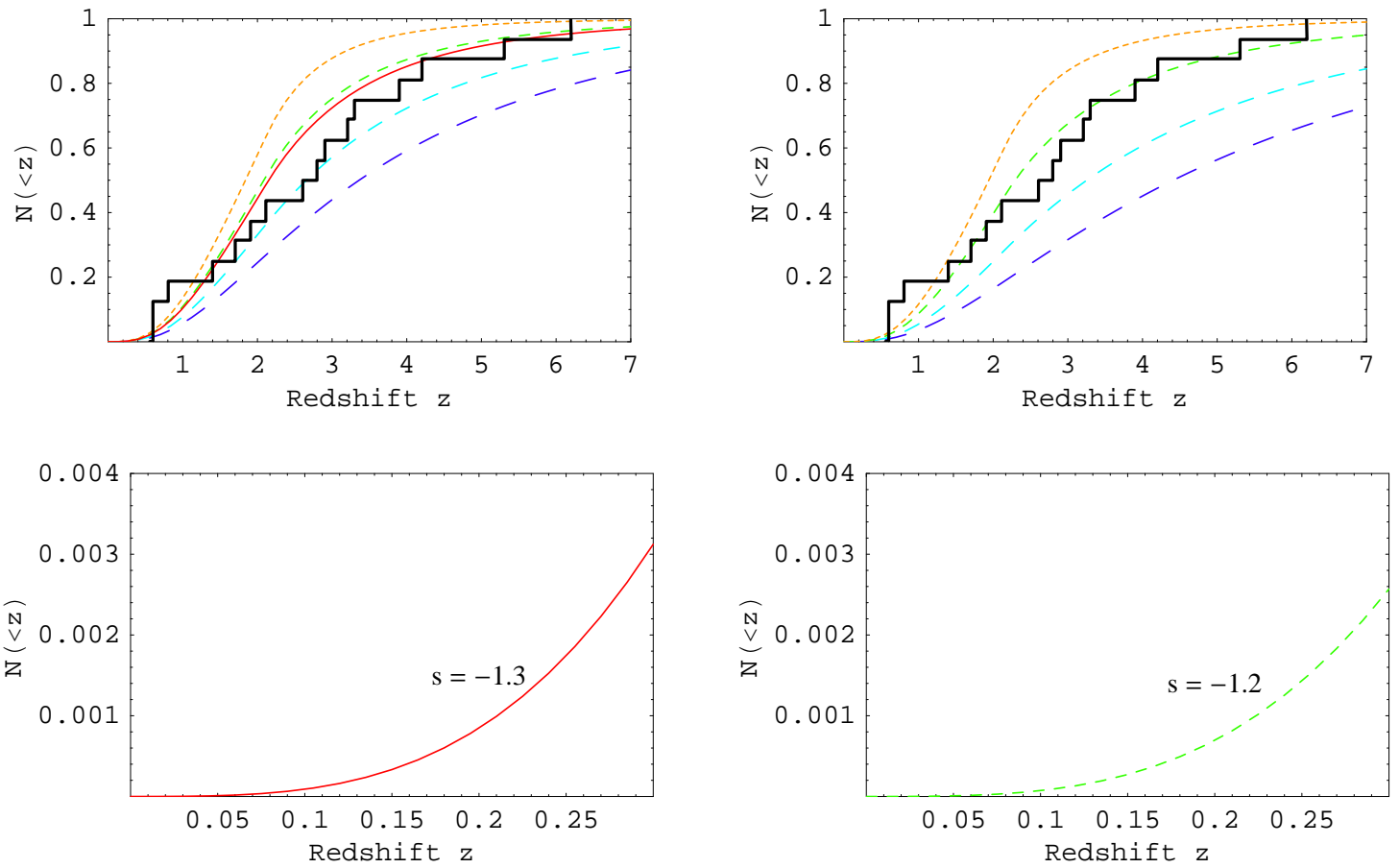


Fig. 23.1 Swift cumulative redshift distribution assuming SFR 5 (left column) and SFR 6 (right column), with $E = 4 \times 10^{51}$ ergs. The two bottom panels show the above best-fitted results at $z = 1$ in more detail.

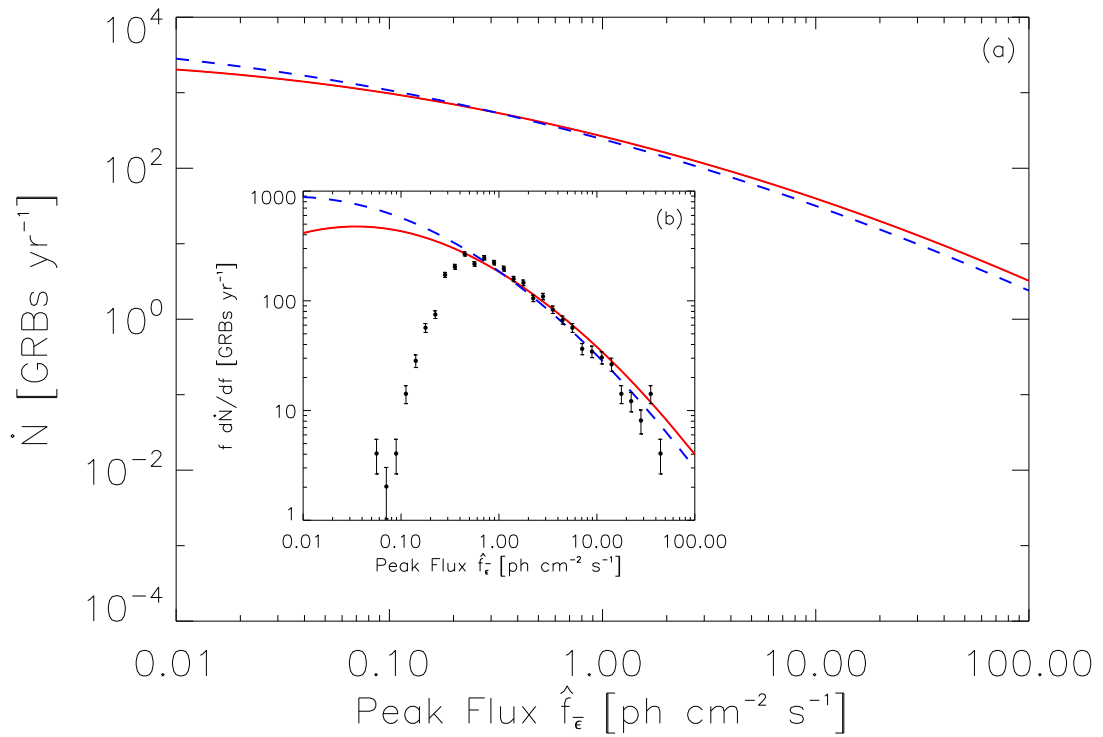


Fig. 24.| Integralsize distributions (a) for SFR 5 (solid) and SFR 6 (dash curve), respectively. The inset is the di erential size distributions (b) for SFR 5 (solid) and SFR 6 (dash curve), respectively. The lled circles curve represents the 1024 m striggertim escale from the 4B catalog data, containing 1292 bursts.

R E F E R E N C E S

Amati, L., et al. 2002, *A & A*, 390, 81

Balogh, Z., et al. 2006, *A & A*, 453, 797

Band, D. L. 2002, *ApJ*, 578, 806

Band, D. L. 2003, *ApJ*, 588, 945

Band, D. L. 2006, *ApJ*, 644, 378

Berger, E., Fox, D. B., Kulkami, S. R., Frail, D. A., & Djorgovski, S. G. 2006, *ApJ*, submitted (astro-ph/0609170)

Berger, E., Kulkami, S. R., Frail, D. A., & Soderberg, A. M. 2003, *ApJ*, 599, 408

Berger, E. et al. 2005, *ApJ*, 634, 501

Blain, A. W., & Narayan, P. 2000, *ApJ*, 312, L35

Blain, A. W. et al. 1999, *MNRAS*, 309, 715

Bloom, J. S., Frail, D. A., & Kulkami, S. R. 2003, *ApJ*, 594, 674

Bottcher, M., & Dermott, C. D. 2000, *ApJ*, 529, 635

Bromm, V., & Loeb, A. 2002, *ApJ*, 575, 111

Bromm, V., & Loeb, A. 2006, *ApJ*, 642, 382

Capellaro, E., Evans, R., & Turatto, M. 1999, *A & A*, 351, 459

Ciardi, B., & Loeb, A. 2000, *ApJ*, 540, 687

Daigne, F., Rossi, E., & Mochkovitch, R. 2006, *MNRAS*, in press (astro-ph/0607618)

Dermott, C. D. 1992, *Phys. Rev. Lett.*, 68, 1799

Dermott, C. D. 2006, *ApJ*, submitted (astro-ph/0605402)

Dermott, C. D., & Holmes, J. M. 2005, *ApJ*, 628, L21

Frail, D. A. et al. 2001, *ApJ*, 562, L55

Friedman, A. S., & Bloom, J. S. 2005, *ApJ*, 627, 1

Fruchter, A. S., et al. 2006, *Nature*, 441, 463

Fynbo, J. P. U., et al. 2006, *A & A*, 451, L47

Gehrels, N. et al. 2004, *ApJ*, 611, 1005

Ghirlanda, G. et al. 2004, *ApJ*, 613, L13

Guetta, D., Piran, T., & Waxman, E. 2005, *ApJ*, 619, 412

Hopkins, A. M., & Beacom, J. F. 2006, *ApJ*, in press (astro-ph/0601463)

Jakobsson, P. et al. 2006, *A&A*, 447, 897

Lamb, D. Q., & Reichart, D. E. 2000, *ApJ*, 536, 1

Liang, E., Zhang, B., Vergili, F., & Dai, Z. G. 2006, *ApJ*, submitted (astro-ph/0605200)

Lloyd-Ronning, N. M., Fryer, C. L., & Ramirez-Ruiz, E. 2002, *ApJ*, 574, 554

Loveday, J., Peterson, B. A., Efstathiou, G., & Maddox, S. J. 1992, *ApJ*, 390, 338

Melott, A. L., et al. 2004, *International Journal of Astrobiology*, 3, 55

Mészáros, P. 2006, *Reports of Progress in Physics*, 69, 2259

Mészáros, P., & Rees, M. J. 1997, *ApJ*, 482, L29

Mészáros, P., Rees, M. J., & Wijers, R. A. M. J. 1998, *ApJ*, 499, 301

Mortsell, E., & Sollerman, J. 2005, *JCAP*, 6, 9

Paciesas, W. S., et al. 1999, *ApJS*, 122, 465

Panaiteescu, A., & Kumar, P. 2001, *ApJ*, 560, L49

Peebles, P. J. E. 1993, *Princeton Series in Physics*, Princeton, NJ: Princeton University Press

Perna, R., Sari, R., & Frail, D. 2003, *ApJ*, 594, 379

Rossi, E., Lazzati, D., & Rees, M. J. 2002, *ApJ*, 332, 945

Spergel, D. N., et al. 2003, *ApJS*, 148, 175

Stanek, K. Z., Gamovich, P. M., Kaluzny, J., Pych, W., & Thompson, I. 1999, *ApJ*, 522, L39

Stanek, K. Z. et al. 2006, *ApJ*, submitted (astro-ph/0604113)

Thomasson, B. C., Jackson, C. H., Melott, A. L., Laird, C. M., Stolarski, R. S., Gehrels, N., Cannizzo, J. K., & Hogan, D. P. 2005, *ApJ*, 622, L153

Totani, T. 1999, *ApJ*, 511, 41

Waxman, E., Kulkami, S. R., & Frail, D. A. 1998, *ApJ*, 497, 288

Wick, S.D., Derm er, C.D., & Atoyan, A. 2004, *Astropart. Phys.*, 21, 125

Wijers, R.A.M.J., Bloom, J.S., Bagla, J.S., & Natarajan, P. 1998, *MNRAS*, 294, L13

Yamazaki, R., Yonetoku, D., & Nakamura, T. 2003, *ApJ*, 594, L79

Zhang, B., Dai, X., Lloyd-Ronning, N.M., & Meszaros, P. 2004, *ApJ*, 601, L119